August 2014

Thermal Cooling Effects in the Microstructure and Properties of Cast Cobalt-Base Biomedical Alloys

Vladimir Vega Valer
University of Wisconsin-Milwaukee

THERMAL COOLING EFFECTS IN THE MICROSTRUCTURE AND PROPERTIES OF CAST COBALT-BASE BIOMEDICAL ALLOYS

by

Vladimir Vega Valer

A Thesis Submitted in

Partial Fulfillment of the

Requirements for the Degree of

Master of Science

in Engineering

at

The University of Wisconsin-Milwaukee

August 2014

ABSTRACT

THERMAL COOLING EFFECTS IN THE MICROSTRUCTURE AND PROPERTIES OF CAST COBALT-BASE BIOMEDICAL ALLOYS

by

Vladimir Vega Valer

The University of Wisconsin-Milwaukee, 2014
Under the Supervision of Professor Hugo Lopez

Joint replacement prosthesis is widely used in the biomedical field to provide a solution for dysfunctional human body joints. The demand for orthopedic knee and hip implants motivate scientists and manufacturers to develop novel materials or to increase the life of service and efficiency of current materials. Cobalt-base alloys have been investigated by various researchers for biomedical implantations. When these alloys contain Chromium, Molybdenum, and Carbon, they exhibit good tribological and mechanical properties, as well as excellent biocompatibility and corrosion resistance.

In this study, the microstructure of cast Co-Cr-Mo-C alloy is purposely modified by inducing rapid solidification through fusion welding processes and solution annealing heat treatment (quenched in water at room temperature. In particular the effect of high cooling rates on the athermal phase transformation FCC(γ)↔HCP(ε) on the alloy hardness and corrosion resistance is investigated.

The Co-alloy microstructures were characterized using metallography and microscopy techniques. It was found that the as cast sample typically dendritic with dendritic grain sizes of approximately 150 μm and containing Cr-rich coarse carbide precipitates along the interdendritic boundaries. Solution annealing gives rise to a refined microstructure with grain size of 30 μm, common among Co-Cr-Mo alloys after heat treating.

Alternatively, an ultrafine grain structure (between 2 and 10 μm) was developed in the fusion zone for specimens melted using Laser and TIG welding methods. When laser surface modification treatments were implemented, the developed solidification microstructure shifted from dendritic to a fine cellular morphology, with possible nanoscale carbide precipitates along the cellular boundaries. In turn, the solidified regions exhibited high hardness values (461.5HV), which exceeds by almost 110 points from the alloy in the as-cast condition.

The amount of developed athermal ε -martensite phase was determined using X-ray diffractrometry. It was found that the amount of ε -martensite increases significantly from 2% for the Laser surface processing to 13% in the as cast specimen, 24% in the annealed specimen, and 51% for the TIG surface processing. Moreover, the corrosion rate in Ringer solution was calculated by applying the Tafel extrapolation method on each alloy condition. The lowest corrosion rate (0.435 μm/year) was achieved in the Laser treated alloy and it is attributed to the lack of appreciable athermal ε -martensite. The highest

corrosion rate (15.5 μm/year) was found to occur in the TIG treated alloy, which possesses the largest amount of ε -martensite.

In turn, this suggests that surface modification through melting induces variable amounts of athermal ε -martensite in the as-cast Co-Cr-Mo-C alloys. Apparently, rapid solidification of melted surfaces in the Co-alloy is highly effective in modifying the induced amounts of HCP phase, and hence, the exhibited properties.

TABLE OF CONTENTS

LIST OF FIGURES

LIST OF TABLES

ACKNOWLEDGEMENTS

First of all, I specially want to dedicate this work thesis to my family. To my mother Silvia who has always supported me throughout my entire life, my brother Ray who has always believed in me without doubting, and my wonderful wife Valerie.

I am deeply grateful to my thesis advisor Dr. Hugo Lopez for being a great mentor and providing me all his expertise during my research.

I would like to thank Dr. Ben Church for all his guidance on academic matter and support during my studies and teaching assistant duties at UW-Milwaukee.

Also, I want to thank Dr. Hardcastle for providing me his time on training and coaching me with much of the equipment at the Advanced Analysis Facility. Finally, I appreciate all the respect and collaboration from my peer teaching assistants and professors in the Materials Department at UW-Milwaukee.

CHAPTER 1. INTRODUCTION

1.1 Problem Statement

Biomedical implant devices became available in the early 1900's with poor success due to the lack of available biomedical materials at the time. Since then, several studies aimed to improve and develop the most suitable material for surgical implantations. Mechanical properties, corrosion resistance, and biocompatibility are the main factors for designing and manufacturing biomedical devices to satisfy those needs. However, depending on the attempted replaced part function, the factors may differ to customize and accomplish design requirements.

Wear debris is the most common problem in hip and knee implants when they replace synovial joint functions in the human body. Limitations in joint movement and movement accompanied by pain lead to new studies to develop more alternatives to fill this gap.

Hip and knee artificial metallic implants were introduced for the first time in the United States by Dr. Austin Moore in the 1940's [1]. Early available materials at the time, such as Steel and Iron, were mostly employed for artificial joint replacements. These materials generated corrosion between the bone and articulations. In addition, materials like Gold and Nickel were also attempted in surgical implants without success because of poor wear resistance. The addition of Chromium and Molybdenum into the steel produced a newly discovered alloy, 316L Stainless Steel, with improved corrosion and wear resistance. Later in the

middle of the 20th century, Titanium and its alloys were used with better properties than the aforementioned alloys [2].

Nowadays, modern techniques and materials have become more available for total hip and knee replacement, and cast Cobalt-based alloys appear to be the best material for this application. According to the American Orthopedic Surgeon [3], only in 2004, 46,000 hip replacements and 40,000 knee replacements were performed in the United States, which shows a great demand for surgical implants for needed patients.

When cast Cobalt is alloyed with Chromium and Molybdenum (also known as ASTM F-75), the mechanical properties of the alloy improve significantly as well as wear and corrosion resistance. Although Sang-Hak Lee has demonstrated that wrought Co-Cr-Mo alloys (ASTM F799) have better mechanical properties than as cast [4], it is important to balance the alloy properties by providing adequate heat treatment and cooling rates to the cast alloy.

The as cast Co-Cr-Mo alloy by nature forms carbide blocks with a coarse dendritic microstructure and other defects, which are formed during the solidification process. Hence, carbide morphology and control in grain refinement are rather important in the final properties of Co-base alloys.

1.2 Objectives of Present Study

The present study provides a deeper understanding of thermal effects in cast Cobalt base alloys and how much the thermally treated alloy differs from its

initial properties. The relationship between the exhibited amount of precipitated hexagonal phase and its corrosion rate under different surface thermal conditions in the alloy were investigated. The goal was to obtain a near 100% FCC matrix with minimal HCP phase under the mentioned conditions. In addition, it was expected to induce grain refinement in the alloy microstructure in order to increase the mechanical strength. In order to obtain the desired microstructure, this study focuses on achieving the following objectives:

a) Provide a grain refinement to the alloy microstructure
b) Promote a near 100% ε-martensitic HCP or FCC phase in the alloy by employing surface fusion techniques, such as Laser and Tungsten Inert Gas (TIG) welding.
c) Understand how the corrosion resistance is affected by the amount of HCP or FCC phase in the alloy.
d) Identify any possible relationships between the generated microstructures and the corrosion resistance of the alloy.

CHAPTER 2. LITERATURE OVERVIEW

2.1 COBALT BASE ALLOYS

2.1.1 Cobalt

Cobalt is an allotropic metal with 2 crystal structures Face Centered Cubic (FCC) and Hexagonal Close Packed (HCP) present in the matrix. In pure Cobalt, the most dominant phase at room temperature is FCC crystal structure and it exhibits a metastable phase above the equilibrium transformation temperature. However, the HCP crystal structure is thermodynamically stable at room temperatures below 417^0C, where the allotropic transformation temperature T_c starts by martensitic transformation. This phenomenon may be caused by the relatively rapid cooling rates during the casting process, where the FCC↔HCP kinetics transformation occurs slowly [5] [6] [7].

2.1.2 Kinetics Transformation Mechanisms FCC↔HCP

In order to understand the FCC↔HCP transformation mechanisms, it is necessary to address some primary concepts.

Defects in crystalline materials, such as dislocations, are necessary to be defined to evaluate the mechanical properties of a material. The concept of dislocations comes from plastic deformation in crystalline materials, where the application of a shear stress to a crystal lattice produces an elastic distortion. Further stressing beyond the yield point leads to dislocation slip along slip systems [8].

In a FCC crystal unit cell, usually dislocation glide occurs in the close packed plane (111) in a $< 110 >$ type direction, and the burgers vector magnitude is $b = \frac{a_\circ}{2} \langle 110 \rangle$. For an HCP unity cell, dislocation glide occurs preferentially along (0001) planes in $\langle 11\bar{2}0 \rangle$ direction with a burgers vector magnitud of $b = \frac{a_\circ}{3} \langle 11\bar{2}0 \rangle$.

Another component which plays a critical role in the case of Ti and its alloys is the Stacking Fault Energy, γ. It can be considered as a surface defect and it is defined as the surface energy associated with a a local interruption in the stacking sequence of the crystal structure. The local displacement is typically seen in planes with ABCABC sequence, such as FCC crystal structures.

In the example of Figure 1, the first layer of atoms on the bottom is denoted as A, the next layer as B, and the subsequent layer on the top as C. If the top layer C creates a direct contact with layer A by depleting layer B, stacking fault in the sequence of ABAB is formed. As a result, the continued addition of more layers creates the Hexagonal Closed Packed crystal structure HCP.

Extrinsic stacking faults refers to when one atom layer disrupts the plane system and it is introduced between the B or C layer. In contrast, when an atom layer is removed in such a way that it alters the plane sequence, it is called intrinsic stacking fault. (See Figure 3).

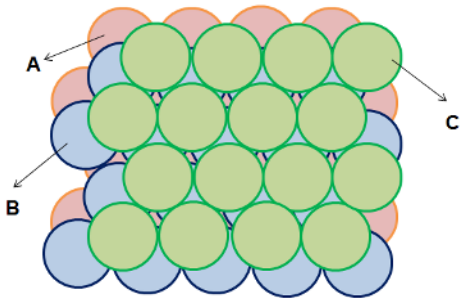

Figure 1. Position of atoms in layers A B C for a face centered cubic crystal (FCC)

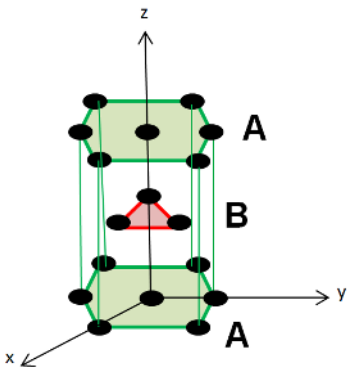

Figure 2. Position of atom layers in a Hexagonal Close Packed crystal structure

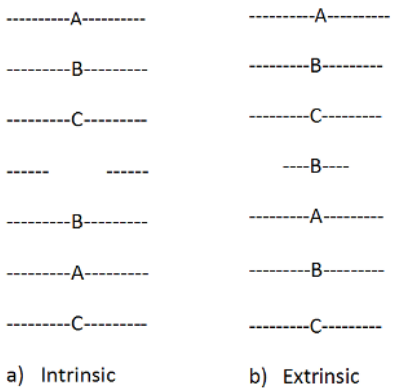

Figure 3. Interruption in the stacking sequence. a) Intrinsic stacking Fault b) Extrinsic Stacking Fault

The energy required to induce a change in the stacking sequence to from FCC to HCP is given by γ. When the magnitude of γ is to large, it is not possible to promote the development of extended dislocations as the energy needed to promote a shift in the stacking sequence is is to large to overcome. A relationship for the conditions needed for a change in stacking sequence can be described by the expression:

$$\gamma_{SFE} = \frac{Gb_2b_3}{2\pi d} \qquad \text{Equation 1}$$

γ = Energy of a stacking fault

G = Elasctic strain energy

b_2b_3 = Scalar product of the Burgers vector

d = distance between burgers vector product

2.1.3 Partial Dislocations

In contrast to stacking fault theory, Shockley partial dislocations will provide a force which favors the spliting of dislocations into extended ones. Due to energy considerations in the elastic strain energy (G= elastic strain energy and b= burgers vector), dislocations can split into shorter magnitude burger vectors unit “b.” For some crystals like FCC, this reaction becomes favorable when γ tends to zero, so the energy barriers are significantly reduced favoring the development of dislocation partials according to the following.

$b_1{}^2 > b_2{}^2 + b_3{}^2$ Equation 2

The burgers vector in an FCC crystal has a dimmension of $\frac{a}{6}[10\bar{1}]$ and split into 2 burgers vectors of magnitude $\frac{a}{6}[11\bar{2}]$ $\frac{a}{6}[2\bar{1}\bar{1}]$ and glide in the (111) slip plane.

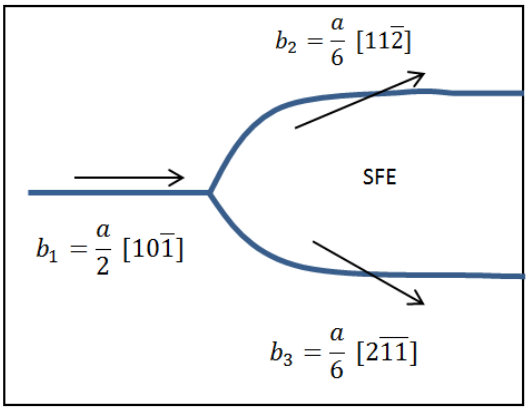

Figure 4. Dissociation of Shockley Partial Dislocations

The scalar product of the partial burgers vectors meets the equation and it becomes energetically favorable to split. The area formed between both partial dislocations is known as the stacking fault energy (SFE).

2.1.4 Cobalt Chromium Molybdenum Alloys

The addition of different chemical elements in Cobalt base alloy, such as Chromium, Molybdenum, and Tungsten help to strengthen the material. Also, small additions of Carbon improve the alloy castability. The Carbon content is essential because it dissolves in the FCC phase providing a solid solution which

together with other alloying elements enhances the strengthening properties of the alloy [9] [10].

Cast Cobalt alloys exhibit a dendritic microstructure with predominant Cobalt FCC-matrix. The dendritic structure is formed with predominant carbides of the type $M_{23}C_6$ blocky carbides and other carbide phases [11] [12]. These blocky carbides are formed during the dendritic solidification in the interdendritic regions at temperatures around 1200°C [11].

Chromium, Molybdenum, and Tungsten lower the stacking fault energy in the alloy and thus help to stabilize the HCP structure. The presence of extended dislocations in low stacking fault Co-alloys causes dislocations to move along the slip planes. Hence in the ε-martensite HCP phase the extended dislocation are unable to easily climb or cross slip directly affecting the mechanical deformation in the alloy [8].

2.1.5 Kinetics Phase Transformation FCC↔HCP in Co-Cr-Mo-C Alloys

Rearragement of the crystal structure and the kinetcs of the transformation exhibited in Co-Cr-Mo alloys can be addressed as a martensitic transformation reaction [10 [13]. A martensitic reaction is the lattice deformation of a crystal in the solid state due to a fault in the plane of close packed structures, and it could be induced by athermal transformations, dislocations, and strain induced nucleation [14].

According to Saldivar and Lopez [15], the FCC↔HCP transformation temperature when the as-cast Cobalt is alloyed with Cr-Mo-C increases in the

range between T_c= 800 to 875°C by isothermal aging. In addition, Saldivar considers that T_c increases to 970°C in wrought Co alloys with low carbon addition (Co-27Cr-5Mo-0.05C) [16]. Therefore when temperatures are induced above the transformation temperatures in the as cast alloy, the interdendritic morphology tends to dissapear and the grains are refined. However, the ∝-FCC phase is retained after the alloy solidifies.

As discussed before, the FCC phase may promote the martensitic HCP phase in Co-Cr-Mo-C alloys if the thermal conditions are met. There are three different methods to induce ε-martensitic HCP phase in the alloy: athermal HCP transformation, isothermal HCP transformation, and starin induced HCP transformation.

2.1.6 Athermal Transformation

In 1976, Vander Sande, Coke, and Wulff [17] proposed that after heat treatment solution annealing in Co-Cr-Mo-C alloys, the FCC phase continue as predominant phase in a metastable state in the alloy microstructure. However, an increment of stacking faults helped to determined the formation of the HCP phase in the alloy. Later in the 1990s, Rostoker and Dvorak [18]. Demonstrated by characterization techniques the formation HCP in Co-Cr-Mo-C alloys after quenched at room temperature from 1300°C.

2.1.7 Isothermal Transformation

Initial stages of the FCC↔HCP transformation was observed by Vander Sande in Co-Cr-Mo- alloys with low carbon content by annealing solution and rapid quench [17]. The small percentage formation of the HCP phase found in the alloy microstructure (approximately 5%) led to investigate the alloy using isothermal aging heat treatment at 650°C to 750°C. It was observed that after long period of time the formation of the ε-martensitic HCP phase was predominant in the alloy (approximately 95%) due to the increment in stacking fault in the FCC phase. Furthermore, Zangeneh, Lashgari, Saghafi, and Karshenas confirmed the same results using isothermal aging temperatures of from 850°C to 950°C as well as the increment in the alloy hardness.

2.1.8 Strain Induced Transformation

The formation of ε-materiste in Co-Cr-Mo-C alloys can be achieved by plastic deformation. The development of fine intergranular striations found in the α-phase corresponds to the nucleation of martensitic HCP phase [19]. In addition, Mani, Salinas and Lopez [20], found that the development of the HCP phase in Co-Cr-Mo-C alloys at room temperature can be induced by applying plastic deformation and it increases by isothermal aging prior elastic straining of the alloy.

2.2 FUSION WELDING THEORY

2.2.1 Definition

Fusion welding is described as a process that joins two metallic materials by involving melting and solidification from both parts. There are three different fusion welding processes in order of heat source increment, and they are classified as the following [21]:

Gas Welding:

- Oxyacetylene Welding (OAW)

Arc Welding

- Shielded Metal Arc Welding (SMAW)
- Gas Tungsten Arc Welding (GTAW)
- Plasma Arc Welding (PAW)
- Gas Metal Arc Welding (GMAW)
- Flux Cored Arc Welding (FCAW)
- Submerged Arc Welding (SAW)
- Electroslag Welding (ESW)

High Energy Beam Welding

- Electron Beam Welding (EBW)
- Laser Beam Welding (LBW)

The two fusion welding processes, which were used in this investigation, were Gas Tungsten Arc Welding and Laser Beam Welding.

2.2.2 Gas Tungsten Arc Welding (GTAW)

GTAW is a fusion welding process that uses a non-consumable Tungsten electrode and melts and joins the metal. The welding process is created by maintaining the electric arc formed by the electrode and the workpiece. Gas Tungsten arc welding is also known as Tungsten Inert Gas (TIG) because the welding process employs a Tungsten electrode to protect the work environment. The Tungsten electrode is connected by a welding cable directly to an electrical terminal and a water coolant system (contact tube) as shown in Figure 5. The environment is shielded or protected by Argon, Helium, or both, and it is fed through the torch. Also, the shielding gas makes contact with the Tungsten electrode to avoid oxidation and contamination from air in the weld.

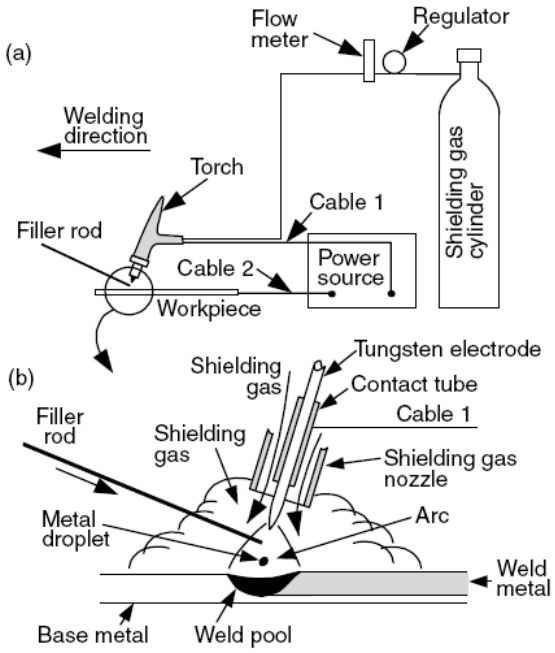

Figure 5. Gas Tungsten Arc Welding process: a) Entire scheme of the welding process. b) Closer view inside the welding area. [21]

Selection of the electrode in GTAW process is very important. Tungsten possesses a relatively high melting point (approximately ~1980ºC) and it doesn't vaporize. Therefore the inconsumable Tungsten electrode will not melt, so it is not used as filler metal during welding as other fusion welding processes do. However, improper operation of the GTAW equipment (wrong current, electrode type, or wrong technique used) may cause melting the electrode and deposition of Tungsten particles in the weld, which creates brittle intermetallic compounds.

Tungsten electrodes may either be pure or alloyed with other elements, such as thorium, zirconium oxide, cerium, or lanthanum. A pure Tungsten electrode provides good arc stability with either Argon or Helium shielding gases. It is commonly used to weld Aluminum and Magnesium. In order to carry high current capacity in the welding process, thorium is added in the electrode. The addition of thorium will provide a desirable electrode with better electron emission quality [22].

One main factor considered for selecting the proper electrode is the type of welding current. There are 3 types of different polarities used in GTAW process: Direct current electrode negative (DCEN), direct current electrode positive (DCEP), and alternating current (AC).

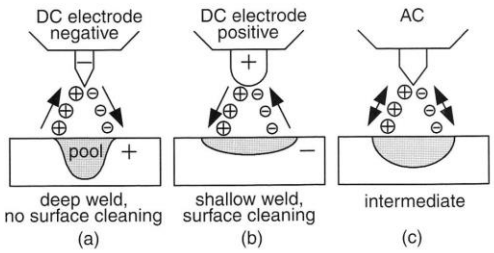

Figure 6. Different polarities used in GTAW process [21].

Direct current electrode negative, also known as straight polarity, is commonly applied to weld almost all metals, except Aluminum and Magnesium. The torch is connected to a negative terminal of the power source and the workpiece is connected to a positive terminal. When the electric arc is created, the electrons will flow from positive to a negative charge. That is why most of the emitted heat (70%) enters to the workpiece and forms a deep penetration in the weld joint.

In contrast, in direct current electrode positive polarity the torch is connected to a positive terminal of the power source and the workpiece is connected to a negative terminal. The electrons will flow in the same manner as DCEN polarity, but now the heat is concentrated in the Tungsten electrode rather than in the workpiece. Because of how the electrons flow, this type of polarity is known as reverse polarity. The weld joint has a small penetration, large fusion zone, and liquid coolant must be employed to avoid melting of the electrode.

Alternating current polarity will change the direction of current flow. The electrode will become positive and the workpiece negative at certain times, and the direction of current flow will alternate to negative at the electrode and positive at the workpiece during another given time. This type of polarity is mostly used to weld Aluminum alloys because it has an intermediate weld penetration and shielding gas protects the workpiece.

The biggest advantage for using the TIG welding process is that it can weld thin sections with limited heat input, and it is widely applied for welding Aluminum, Magnesium, Copper, Stainless steel, etc. Other advantages for

considering TIG process are high weld quality, deep penetration with small HAZ region in the weld joint, control of current and energy input, less distortion, and no smoke or sparks during the welding process. However, increasing the welding current may cause dissolution of the Tungsten electrode and promote brittle intermetallic inclusions in the weld joint.

2.2.3 Laser Beam Welding

Lasers have been developed since the postulation of emission of stimulated electrons and quantum mechanics principles in the 20th century. Lasers continued the interest in physics until 1970s. In the 1980s, Laser beam welding became available in the solid state and CO2 state for the production of metal working. Since then, the efficiency of LBW for joining metals has become more attractive and interesting to the welding industry.

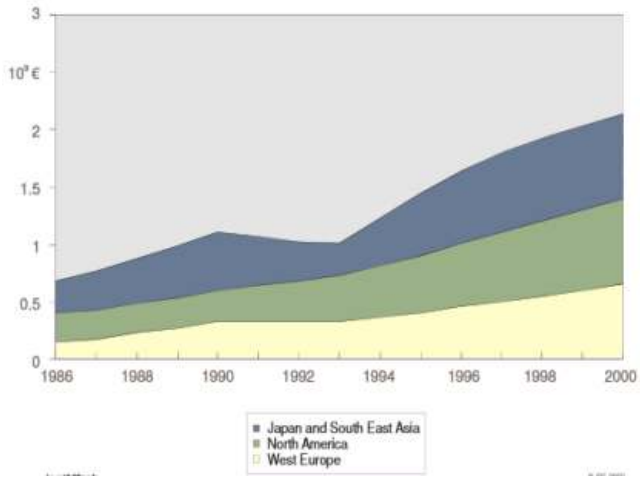

Figure 7. Development of LBW process in the market from 1980's to the 2000's [23].

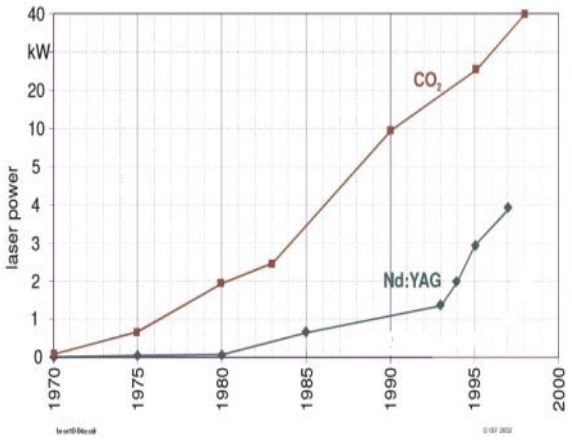

Figure 8. Development of Laser sources throughout the years [23].

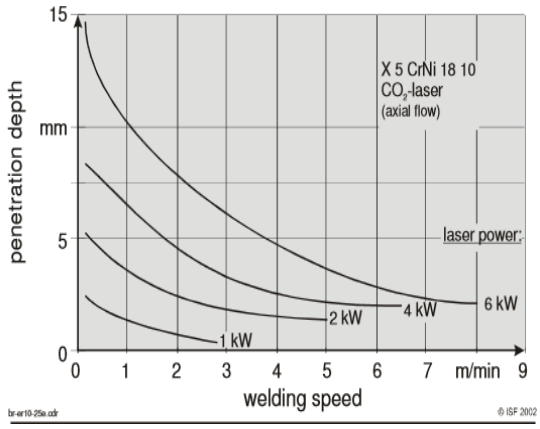

Figure 9. Weld penetration of CO2 Laser at different power sources [23].

Laser Beam Welding is a technique that melts and joins metals by applying high power density. A scheme in Fig. 9 shows the penetration depth of CO2 Laser welding at different power sources.

LBW can be in solid state laser, gas state laser, and semiconductor or diode laser. The reason for using CO2 laser is based on the quality and speed of welding on some materials like Nitinol.

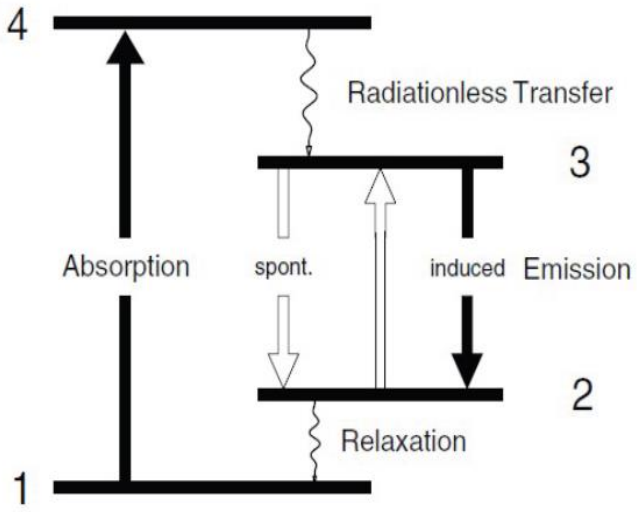

Figure 10. YAG Four level laser welding system [24].

In solid state laser, the Yttrium Aluminum Garnet (YAG) single crystal is doped with Neodymium. Gas molecules become excited from ground state level (1) to higher energy levels (4) due to high input intensity. The laser transition from state (3) to state (2) occurs once the Neodymium ions decay to level (2) and they quickly relax back to the ground state to begin the process again. The energy released in the form of photons is called laser.

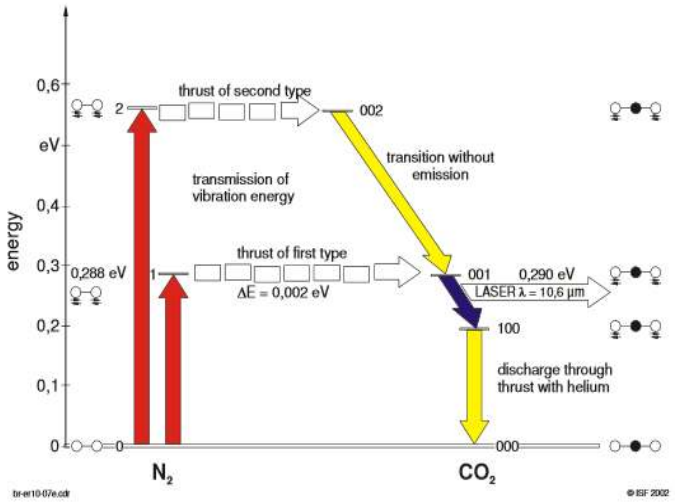

Figure 11. CO2 Laser diagram [24].

Similar to the concept in YAG laser, gas state laser follows the same principle with the exception of a gas mixture of N2, CO2, and He that are employed. The difference between YAG and CO2 lasers is that in CO2 state Nitrogen molecules will excite CO2 molecules to emit energy, and finally He atom will stabilize CO2 atoms to lower energy states.

LBW is commonly used in open environments, and the use of gas shielding is highly recommended to protect the weld from oxidation and contamination. If shielding gas is avoided, the laser beam will be ionized and absorbed by the plasma formed during welding. This phenomenon contributes to minimized depth of penetration; therefore removing plasma is necessary to apply shielding gas, such as Helium or Argon. Argon will be chosen for better results in depth of penetration because the ionization of Helium is more achievable than in Argon due to high energy ionization of He (24.5 ev) compared with Ar (1.5 ev) [25].

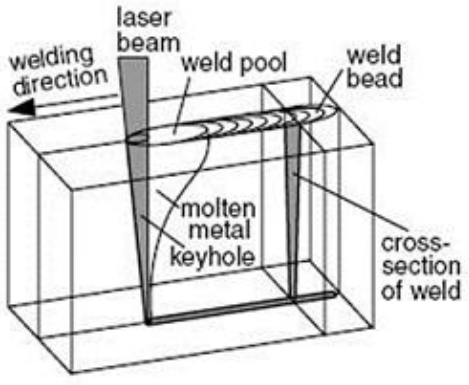

Figure 12. Electron Beam Welding process [21]

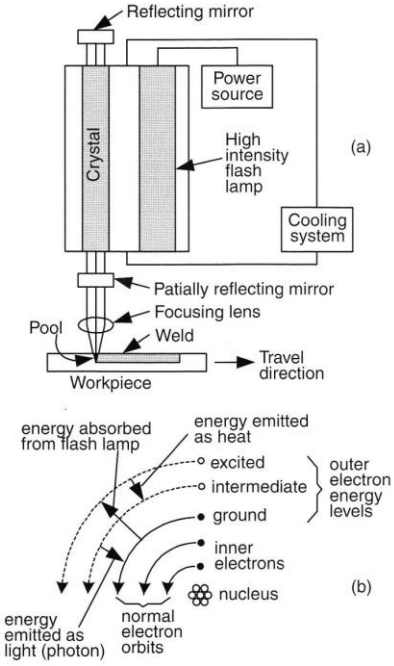

Figure 13. Energy released by electron emission in Laser beam welding [21].

Some advantages of using LBW are:

- Process: High power density, small beam diameter, high welding speed, noncontact between the nozzle and the metal.
- Work piece: Minimum thermal stresses, little distortion, materials can be welded at different positions.
- Installation: Short cycle times, several operation stations can be possible, simple automatic installation.

However, the surface should be modified by roughening, oxidizing, or coating in the metal in order to avoid high reflectivity of the laser beam, especially if the metal is polished. Also, the equipment is expensive and high skilled operators are needed to obtain high quality results in the weld.

2.2.4 Heat Flow

Once fusion welding process is applied to metallic materials, the power density of the heat source will cause a change in the weld joint. Fast solidification from the liquid to solid state in the weld pool may promote a different phase in the microstructure, as well as different grain size. In order to control or take advantage of physical properties in the solidified region, it is important to understand the relationship between power density and heat source.

The heat source depends on the welding process that is being used, and it could produce a narrow and deep penetration keyhole (high energy welding process) to a wide and not fully weld penetration (gas welding processes). The difference on both processes is how much heat has been introduced and spread over the workpiece. In Figure 14, the relationship between heat input and power density of the heat source in LBW shows that the gas flame may produce damage to the workpiece due to the slow conduction of heat to the workpiece. On the other hand, high energy beam welding process conducts the heat and melts a localized area on the workpiece, which results in a high quality weld joint. However, high energy beam welding melts and solidifies the metal so fast that some elements, such as Mg and Pb may vaporize and damage the vacuum system [21].

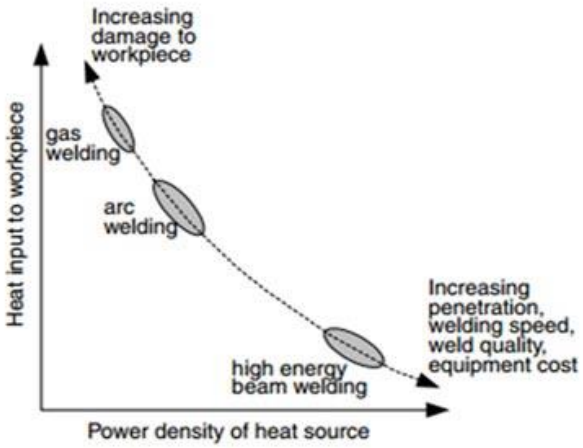

Figure 14. Scheme of fusion welding processes according to the heat source and heat input introduced in the workpiece [21].

2.2.5 Fusion Zone

The final properties of the weld joint are directly related to how the metal solidifies and promotes the microstructure in the weld pool. The weld microstructure contains 3 different zones: the fusion zone, the heat affected zone, and the base metal.

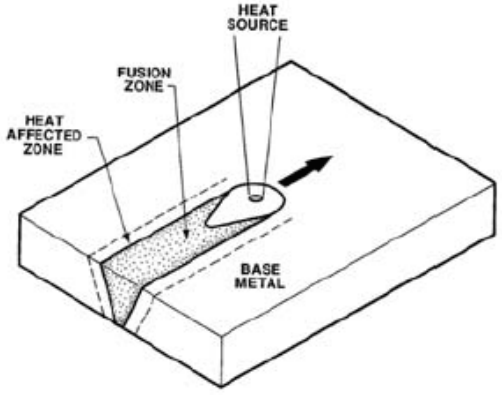

Figure 15. Three different zones produced during fusion welding [21]

The fusion zone is formed when the welding temperatures reach the liquidus phase in the base metal and it solidifies, creating a new localized microstructure. It is very important to understand the effect of solidification in the weld because it will determine the final microstructure morphology, grain size, solute redistribution, inclusions, etc. Therefore an uncontrolled solidification of the melt in the fusion zone is associated with defects and flaws, such as residual stresses, porosity, cracks, and distortion.

Solidification in metal alloys occurs at the liquid solid interface, and it starts when the freezing temperature reaches a thermodynamic equilibrium, $\Delta G_l = \Delta G_s$ where ΔG_l is the free energy in the liquid and ΔG_s free energy in the solid, and the freezing temperature is defined as "the temperature at which the free energy of the solid phase equals that of the liquid" [26]. Freezing in metal alloys is promoted by nucleation and growth process, where the nuclei forms first and then it leads to grow as a dendrite to finally form grains. The formation of new granular crystals during solidification depends on the S/L interface breakdown process. When the actual liquid temperature is below the liquidus temperature, segregated rich solute builds up and creates a boundary layer at the S/L interface. The difference between both temperatures is called the freezing range $\Delta T = T_l - T_s$ and the thickness of the boundary layer is D_l/R. If a tangent is drawn across the liquidus temperature at the S/L interface, a relationship between the freezing range and the growth rate is calculated, which is followed by:

$$\frac{G}{R} \propto \frac{\Delta T}{D_l}$$ Equation 3

Where:

$G =$ Actual temperature gradient

$R =$ Growth rate

$\Delta T =$ Freezing range

$D_l =$ Diffusion coefficient in the liquid

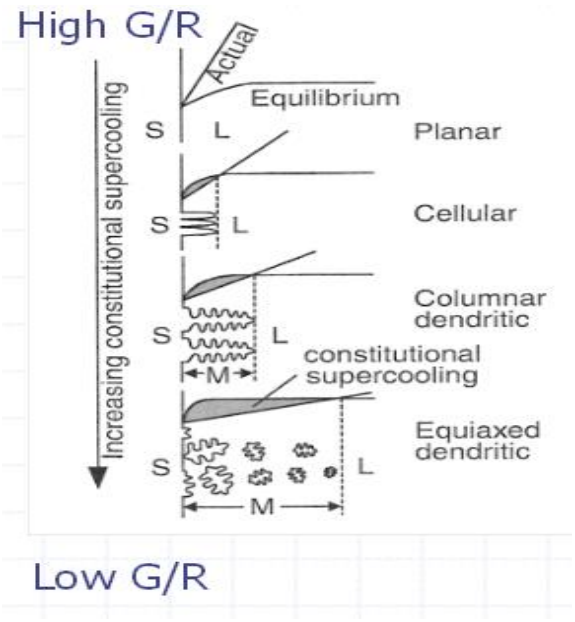

Figure 16. Development of the solidification mode by the effect of constitutional supercoiling and the temperature gradient and growth rate [21].

2.2.6 Constitutional Supercooling

Constitutional supercooling is given by the ratio G/R and it determines the morphology at the S/L interface after solidification. There 4 modes of solidification: planar, cellular columnar, and equiaxed as seen in Figure 16. Fast

solidification rates lead to a fine microstructure (equiaxed) while slow cooling rates or high G/R promote a planar microstructure.

2.2.7 Weld Grain Structure

As mentioned before, the morphology of the microstructure, grain size, and solute redistribution is controlled by the growth rate and temperature gradient G/R. Grain growth is dominated by the solidification of the weld, and it tends to grow opposite to the heat direction [21]. However, the welding speed is a very important parameter to consider because it provides the cooling time rate needed for solidification. In other words, as the weld speed increases, the constitutional supercoiling increases as well leading to an epitaxial solidification mode. On the other hand, if the weld speed is reduced, most likely columnar solidification mode takes place on the weld pool microstructure (See Figure 17).

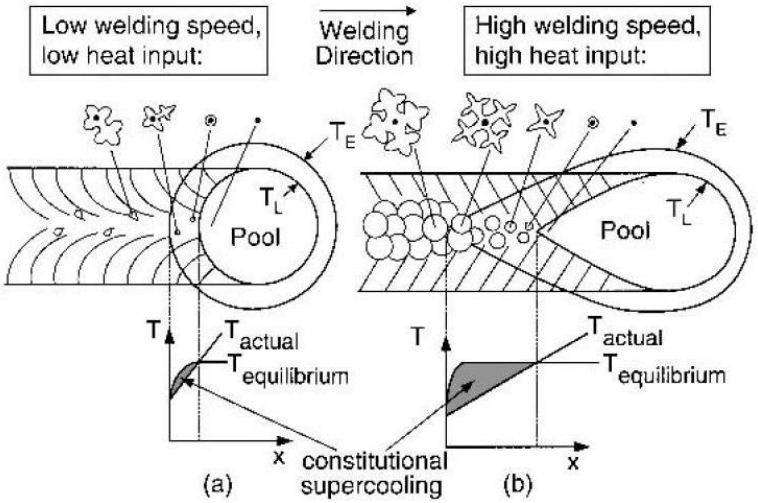

Figure 17. Weld speed and constitutional supercoiling effect on the weld microstructure. a) Low welding speed. b) High welding speed [21].

2.3 Corrosion Theory

2.3.1 Definition

Corrosion is the electrochemical reaction of a material when it is exposed to a corrosive environment that results in its deterioration. There are four requirements for a corrosion cell to initiate the electrochemical reaction process:

- Anode
- Cathode
- Ion path
- Electron path

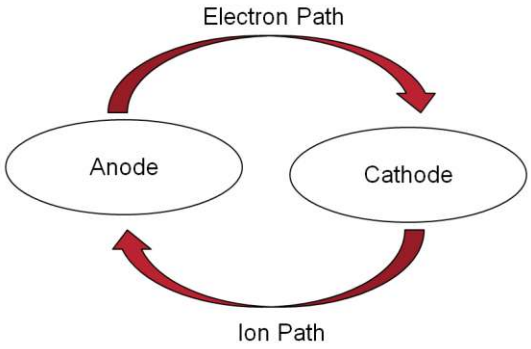

Figure 18. Schematic diagram of a corrosion cell showing the electrochemical reaction processes [27].

At the anode metal atoms will change from solution into ions in the form of oxidation reaction, and here is where corrosion will initiate. On the other hand, the cathode, metal atoms are consumed in the form of reduction reaction, and no corrosion takes place.

The following corrosion mechanisms are typically found in deterioration of metallic materials:

- Uniform: When a corrosive environment gets access to the entire metallic material and causes general corrosion on the surface of the metal.
- Galvanic: Two dissimilar metals are in contact with each other in the presence of a certain environment. One of them will corrode while the other performs resistance to corrosion.
- Crevice: Form of corrosion deposited in a crevice created by contact with another metal. The anode is isolated in the crevice surrounded by a passive surface acting as a cathode.
- Pitting: Localized corrosion formed by the attack of an electrolyte to the metal surface. It is caused by the breakdown of the metal protective film at isolated sites.
- Environmentally Induced Cracking
    - Stress Corrosion Cracking: When static load stresses under a corrosive envirnoment cause uniform corrosion.
    - Hydrogen Induced Cracking: Decarburization is a typical mechanism of hydrogen attack in carbon steels created by the diffusion of hydrogen ions and may cause embrittlement in the metal alloy.
    - Corrosion Fatigue Cracking: It is caused by cycle stresses in a corrosive environment.

- Intergranular: When corrosion attacks at the grain boundaries due to depletion of certain alloying elements. A classic example is sencitization in stainless steel, where Chromium is depleted from the matrix and exposes the material to corrosion.
- Dealloying and Dezincification: Some examples are the the depletion of Zinc ions from brass.
- Erosion: The movement of a corrosive fluid attacks and removes the metal alloy protective film creating erosion corrosion.
- Fretting: Is initiated by repeated small movements, usually vibration, in a corrosive environment, and breaks the protective film from the surface of a metal alloy.

The mechanisms of corrosion are a function of kinetics, thermodynamics and difussion mechanisms. The basic process of corrosion in metallic materials involves electron transfer, and it is shown in Figure 19 where a metal M is exposed in Hydrochloric solution HCl.

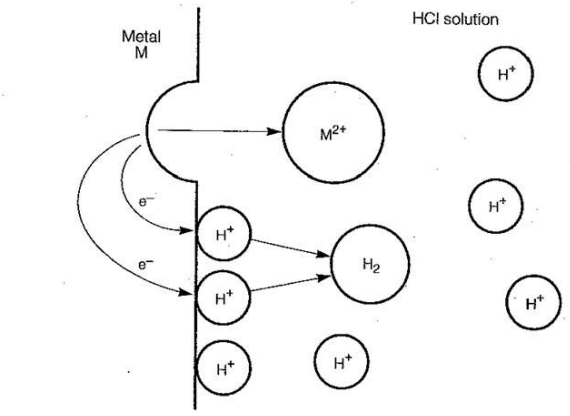

Figure 19. Image of electron transfer mechanism of a metal under a corrosive environment [27]

The anodic oxidation of the reactive metal M^{2+} causes the Chloride atoms to break in a form of cathodic oxidation, the corrosion reaction and it is given by the equation:

$$M \rightarrow M^{2+} + 2e^{-} \qquad \text{anodic reaction}$$

$$2H^{+} + 2e^{-} \rightarrow H_2 \qquad \text{cathodic reaction}$$

$$xM + yHCl \rightarrow M_x Cl_y + yH^{+} \qquad \text{corrosion reaction}$$

The corrosion reaction is associated with the change in free energy ∆G and the electrochemical potential E by the following equation:

$$\Delta G = -nFE \qquad \text{Equation 4}$$

Where:

$\Delta G =$ Change in free energy

$n =$ number of electrons

$F =$ Faraday constant 96,500 Coulombs

$E =$ Electrode potential

When the change in free energy is negative, the reacted products have lower energy than the reactants. Therefore there is a spontaneous reaction involving an exchange or transfer of electrons. The electrode potential will be given by the sum of the potentials for each half cell reaction, the anodic potential (e_a) reaction plus the cathodic potential reaction (e_c).

$$E = E_a + E_c \qquad \text{Equation 5}$$

The reaction rate is caused by the electron transfer during oxidation and reduction reactions, and it is known as the exhange current density i. The

exchange current density is an experimental term that cannot be calculated from theoretical principles.

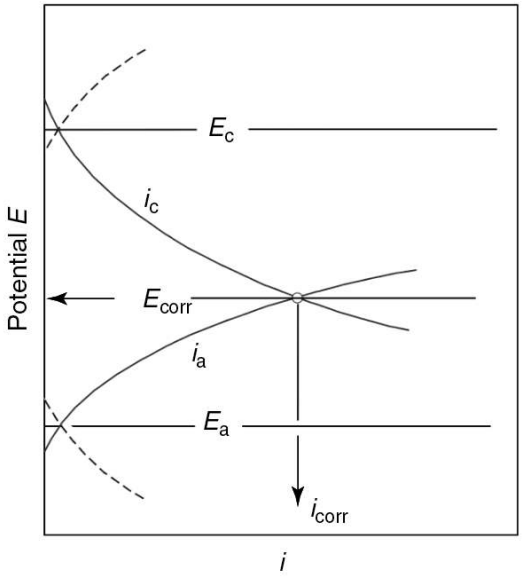

Figure 20. Polarization curve between Electrode potential “E” and the Current density “i” [28].

The relationship between the electrode potential E and the exchange current density i of both the anodic reaction and cathodic reaction curves are governed by corrosion kinetics, which describe the polarization curves of corrosion reactions.

The interpolated point from the anodic and cathodic polarizations curves represents the corrosion current i_{corr} and the corrosion potential E_{corr} respectively (Figure 20).

In order to better understand the term polarization, lets assume equation 5 and figure 21, the difference in electrode potential $E - e$ is caused by a deviation from the equilibrium half cell reaction, and it is named polarization η. The

electrons from the metal M are removed in the form of anocid reaction M^{2+}; as a result there is a positive electrode potential change which is known as anodic polarization η_a. For cathodic polarization η_c, the electrons supplied to the metal surface cause a negative electrode potential change [27].

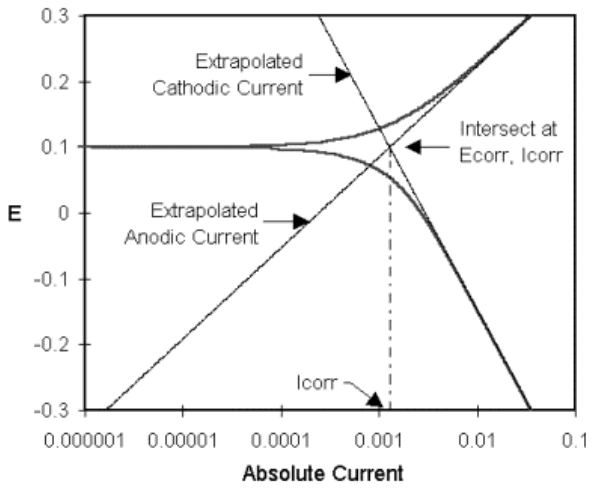

Figure 21. Anodic and cathodic polarization reactions [27].

$$\eta_a = \beta_a \log \frac{i_a}{i_\circ} \qquad \text{Equation 6}$$

$$\eta_c = \beta_c \log \frac{i_c}{i_\circ} \qquad \text{Equation 7}$$

The Tafel constant β could be positive or negative depending on the half-cell reaction. As mentioned above, the anodic overpotential η_a is positive, therefore the Tafel constant for the anodic half-cell reaction β_a must be positive, and the Tafel constant for the cathodic half-cell reaction β_c is negative due to the negative value of the cathodic overpotential η_c.

2.3.2 Passivity

The formation of a protective oxidized thin film of metallic materials with high anodic polarization in corrosive environments is called “passivity” [27]. Most metals behave differently as the anodic polarization and electrode potential increase. Figure 22 demonstrates how the passive film and the active, passive, and transpassive regions are formed in the anodic and cathodic polarization curves.

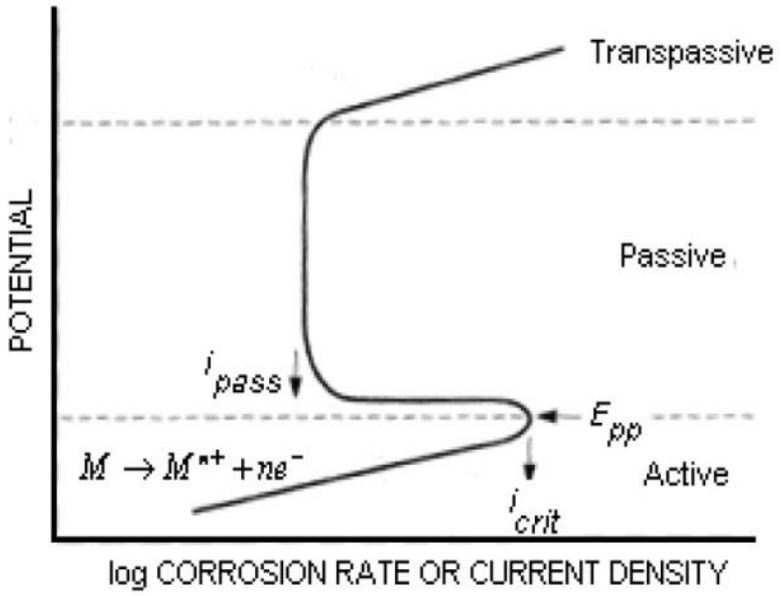

Figure 22. Corrosion passive film protection [27].

The current density increases at very low electrode potentials within the “Active region” to a certain electrode potential E, which is known as passivation potential $E_{\square p}$, and current density i_{crit} where the oxide film becomes stable and the anodic metal passivation decreases drastically. In the passive region, the stable passive film grows in thickness at anodic potential at rates of 1nm to 3nm V−1 equivalent

to an electric field of 106 to 107 V cm−1 across the film [29] and the corrosion rate decreases i_{pass}. Once the oxidized passive film becomes unstable and the anodic potential and current increase, the transpassive region is formed again near the oxygen evolution potential.

2.3.3 Corrosion Rate Measurement

There are three methods to measure corrosion rate, a conventional uniform corrosion rate by weight loss, Tafel extrapolation and polarization resistance. The last two methods are measured by electrochemical polarization and take much less time than weight loss uniform corrosion measurement.

2.3.4 Weight Loss Method

Uniform corrosion rate measurement by weight loss method is conducted in a laboratory using specialized equipment to simulate and reduce the time of exposure in corrosive environments. The specimens are exposed to the corrosive environment for a long time in order to obtain sufficient corrosion product. Then corrosion rate is calculated from the coupon weight loss, followed by metallographic examinations to identify localized forms of corrosion [27]. Corrosion rate formulas are given by:

$$MPY = \frac{534\,W}{D\,A\,T} \qquad \text{Equation 8}$$

$$\mu m/yr = \frac{87600\,W}{D\,A\,T} \qquad \text{Equation 9}$$

Where:

$MPY =$ Corrosion rate in mil per year (1 mil is a thousand of an inch: 0.001in)

$\mu m/yr =$ Corrosion rate in micrometre per year

$W =$ Corrosion weight loss in milligrams

$D =$ Density in grams per cubic meter

$A =$ Area in square inches

$T =$ Time in hours

2.3.5 Tafel Extrapolation Method

The Tafel region is obtained by extrapolating the anodic and cathodic polarization currents (see Figure 21), and at this point the extrapolated corrosion potential E_{corr} corresponds to the corrosion rate i_{corr} in terms of current density. This method is more is accurate under ideal conditions than the weight loss corrosion rate method. Also, Tafel plots have the advantage of measuring very low corrosion rates and help scientists to determine fast corrosion rates using inhibitors.

2.3.7 Polarization Resistance Method

In this method the applied exchange current density is a linear function of the electrode potential. From equations 6 and 7 the polarization resistance R_p can be obtained in terms of corrosion rate (i_{corr}).

$$R_p = \frac{\Delta E}{\Delta i} = \frac{\beta_a \beta_c}{2.3(\beta_a + \beta_c) i_{corr}} \qquad \text{Equation 10}$$

$$R_p = \frac{\beta_a \beta_c}{2.3(\beta_a + \beta_c)} \qquad \text{Equation 11}$$

$$R_p = \frac{B}{i_{corr}}$$ Equation 12

It is important to mention that the polarization resistance method uses the plot of $\Delta E \ vs \ \Delta i$. Also, it can measure corrosion rates at each reading during the test. In other words, it can be completed in a very short period of time. If the $\Delta E \ vs \ \Delta i$ plot is curved, the polarization resistance R_p can be obtained by drawing a tangent line to the curve at the corrosion potential E_{corr} and at zero current density.

CHAPTER 3: EXPERIMENTAL PROCEDURE

3.1 Cast Co-Cr-Mo-C alloy Process

In this investigation, the studied material is cast Cobalt Chromium Molybdenum alloy, also known as ASTM F-75. It is part of a combined work by the Mexican Corporation for Research in Materials (COMIMSA) in Saltillo, Coahuila, Mexico, the Amirkabir University of Technology in Tehran, Iran, and the University of Wisconsin Milwaukee, United States. The Co-Cr-Mo alloy was processed by using an investment casting technique, thermally treated by fusion welding, and delivered by COMIMSA (Saltillo, Mexico) to understand the thermal effect of the alloy microstructure on its corrosion resistance.

In order to make the investment mold prior to pouring the molten metal, a pattern shape of the component was designed. The desired pattern shape was made of plaster, then layered with liquid wax, and assembled onto a sprue system that creates the final tree or mold required for investment casting. Each desired pattern, which is the exact replica of the component, has dimensions of 2 cm length, 2 cm width, and 0.8 cm thickness. The pattern is covered by liquid wax; once the wax is dried, the pattern will be extracted. This procedure is repeated many times to create several patterns. The feeding and gate system is also made of plaster, and it will be layered with liquid wax and extracted the same as all the other patterns. In order to create the final mold required for investment casting, the wax molds are assembled one by one onto the sprue. The tree is submerged into ceramic slurry and then covered by dry sand for six

times to produce six ceramic layers to then provide the final ceramic mold. The ceramic mold is taken to a furnace to dewax and to add resistance to the final mold. The chemical composition of the as cast Co-Cr-Mo-C alloy is described in table 1 in accordance with ASTM F75/12 standard.

Elements	Cobalt	Chromium	Molybdenum	Carbon	Silicon
Required	Balance >34	27 to 30	5 to 7	0.35 max.	1.5 max.
Experimental	Balance	28	5	0.3	1.5

Table.1 Chemical composition of as cast ASTM F75 alloy [30].

3.2 Welding Process

The cast Co-Cr-Mo-C alloy surface was thermally treated by two different fusion welding techniques: Laser Beam Welding (LBW) and Gas Tungsten Arc Welding (GTAW)

Laser surface treated samples were sent by COMIMSA in the following conditions:

a) As cast Co-Cr-Mo-C alloy in accordance with ASTM F75 standard. Table1
b) The as cast Co-based alloy ingot was sectioned in cylindrical disc shapes using waterjet equipment with dimensions of 3.92 cm in diameter by 0.70 cm in width. The sectioned samples were ground up to 1200 SiC grit paper. To avoid surface reflection, samples were sand abrasive.
c) Laser Beam Welding technique was employed to provide laser melting spots on the surface of the as cast Co-based alloy.

- Nd:YAG pulsed laser model HTS LS P-160 with a 1064 nm wavelength.
- The welding environment was protected by Argon gas (1.5 L/min) to avoid metal oxidation.
- A laser beam spot has a diameter of 0.8 ± 0.05 mm on the work piece.
- The pulse frequency for all the tests was fixed at $8s^{-1}$.
- Laser beads were overlapped 50% on top of each other. A schematic representation of the LSM process on the disc plates is shown in Figure 23.

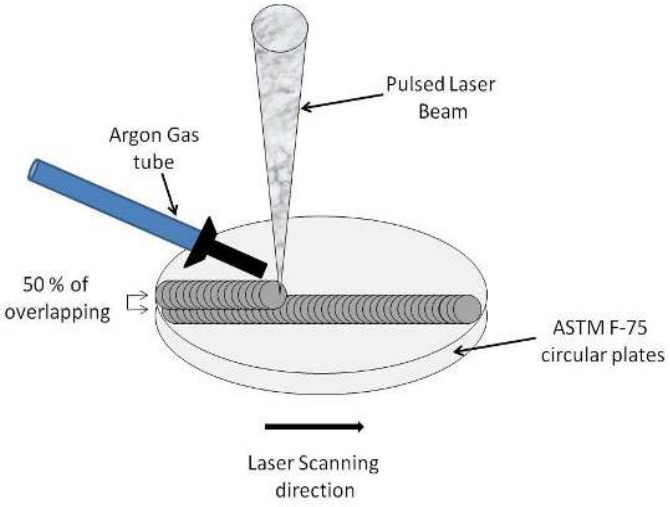

Figure 23. Schematic representation of the LSM process on the Co-Cr-Mo alloy disc plates [42]

Amirkabir University of Technology, Tehran, Iran has supported this investigation by thermally modifying the surface of the as cast ASTM F75 alloy

using the GTAW technique. The following solution heat treatment and welding parameters in the alloy were employed:

a) An as cast Co-Cr-Mo-C alloy ingot of similar composition as mentioned in Table 1 after a solution heat treatment at the temperature of 1230 $\pm 5^0$C for 3 hours in a tubular furnace under Argon inert gas atmosphere, followed by quenching in water at room temperature.
b) The heat treated alloy was cut into rectangular plates with dimensions of 100 mm, 25 mm, and 4 mm respectively.
c) GTAW process was employed to promote melt on the heat treated sample surface by using Miller TIG torch with a constant voltage of 15V and 110A of current. A TIG torch speed of 180 mm/min was used on a sample subjected to no mobility, and protected by Argon gas.

3.3 Metallographic Sample Preparation

First, all samples were cross sectioned and mounted in an automatic mounting press Buehler Simplimet 1000. The metallographic samples were prepared by mechanical polishing in Silicon Carbide paper 400, 600, 800, and 1200 followed by cloth polishing in 1µm and 0.5µm of Al_2O_3 respectively. The sample was electrolytic etched in a solution of 10gr. $FeCl_3$ 5ml. HCl and distilled water at 4 volts for 10 seconds (Figure 24).

Figure 24. Electroetching equipment Buehler Electromet

3.4 Micro-hardness Test

A Micro-hardness test was carried out using a Buehler Micromet II digital micro-hardness tester. The hardness readings were taken from the weld pool surface edge to the core of the sample. Each indentation was separated 0.005 inch from each other, and they crossed through the Heat Affected Zone until the base metal was reached.

Figure 25. Buehler Micromet II digital micro-hardness tester

3.5 Optical Microscopy

In order to observe the alloy microstructure, Zeiss Axio Vert.A1 Optical Microscope was utilized.

Figure 26. Optical Microscope Zeiss Axio Vert.A1 (left) and Stereo Microscope Zeiss (right)

3.6 Scanning Electron Microscopy

The alloy microstructure and quantitative chemical analysis of all specimens were performed using a Topcon SM300 Scanning Electron Microscope at 20KV of intensity.

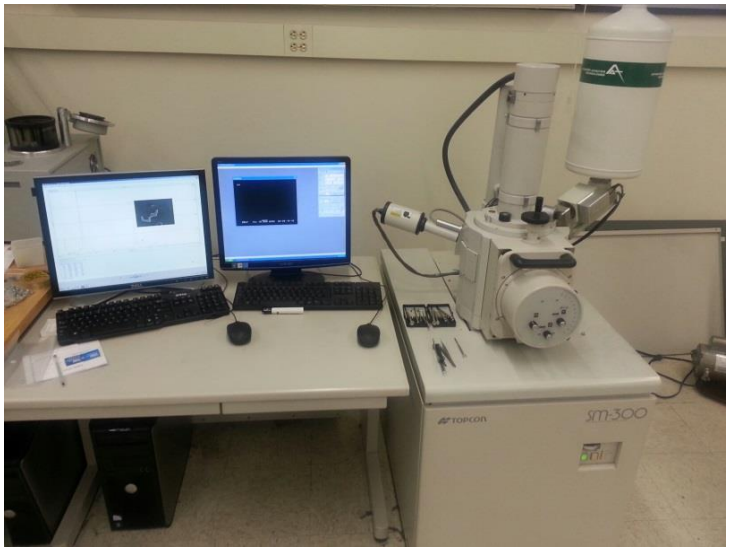

Figure 27. Topcon SM300 Scanning Electron Microscope equipment with incorporate EDS analysis

3.7 X-Ray Diffraction

The XRD equipment used for this investigation was a Bruker D8 Discover X-Ray Diffraction using Cu Kα radiation and 40KV primary beam at the 2θ range of 35^0 to 55^0 at room temperature. The quantity of phase transformation FCC↔HCP was determined from the integrated X-Ray diffraction patterns.

Quantitative calculations of the developed HCP phase in the alloy microstructure was proposed by Sage and Guillaud [31], They suggest to take into account only the diffraction patterns corresponding to $(200)_{FCC}$ and the $(10\bar{1}1)_{HCP}$ because they are the only well distinguished and not overlapped diffraction patterns at a given 2θ. The formula to calculate quantitatively the FCC↔HCP phase transformation in Co-Cr-Mo-C alloys is:

$$\frac{1-x}{x} = 1.5\frac{I_{(200)_{FCC}}}{I_{(10\bar{1}1)_{HCP}}} * 100 \qquad \text{Equation 13}$$

Where:

x = HCP volume in weight percent

$I_{(200)_{FCC}}$ = Integrated area of the intensity peak for the cubic phase

$I_{(10\bar{1}1)_{HCP}}$ = Integrated area of the intensity peak for the hexagonal phase

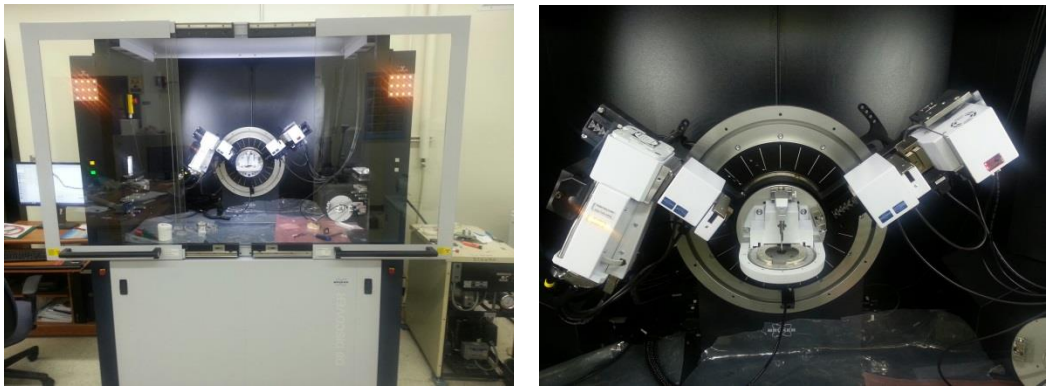

Figure 28. Extended scheme of the Bruker D8 Discover X-Ray Diffraction equipment (left). A closer look of the X-Ray source and detector (right).

3.8 Corrosion Test

The corrosion rate in the alloy was measured by interpolating potentiodynamic curves. The instrument used for test corrosion was VoltaLab PGZ 100. A saturated calomel electrode (SCE) model RE-2B was employed as an electrode reference. The galvanic corrosion cell was protected by Argon gas and the specimens were immersed in Ringer solution (1L distilled water, 8.6 gr.$NaCl$, 0.33 gr. HCl, and 0.30 gr. $CaCl_2$)

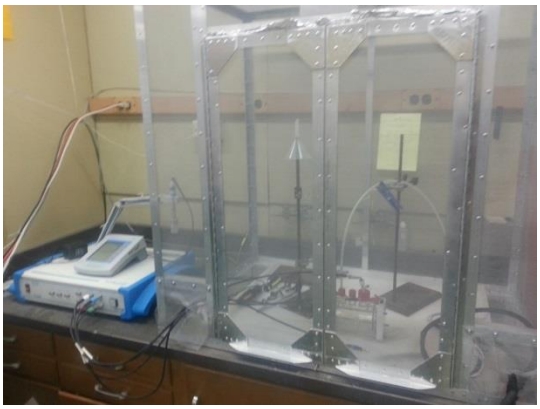

Figure 29. Isolated system equipment for the corrosion test

Figure 30. Installation of the corrosion cell system

Figure 31. VoltaLab PGZ 100 corrosion test equipment

CHAPTER 4. RESULTS AND DISCUSSION

4.1 Microstructure

4.1.1 As received Cast Cobalt-base Alloy

Defects, such as porosity, were identified in the as cast microstructure, which are typical of casting structures as shown in Figure 33.

The as cast alloy was found to contain coarse blocky carbide precipitates of approximate 25 µm to 200 µm in size with dominant $M_{23}C_6$ carbide type at interdendritic regions in the alloy microstructure. Although Kilner [33] has reported lamellar pearlitic regions containing α-FCC phase and M6C3 carbide type in cast Co-Cr-Mo alloys. EDS analysis demonstrate Co and Cr as dominant elements in the matrix, which are associated to the α-phase (Figure 37). Also, pearlitic-like lamellar regions were found in the carbide morphology, where the content of Cobalt reduces as Molybdenum and Chromium increases significantly (Figure 38).

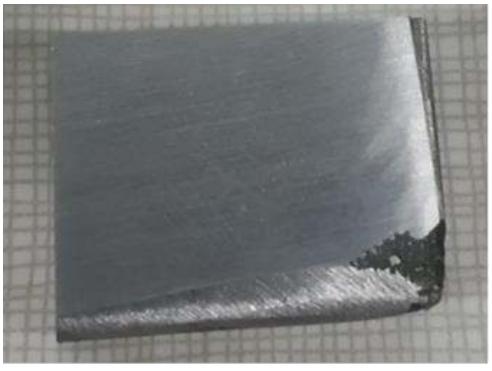

Figure 32. As received cast Co-Cr-Mo-C alloy

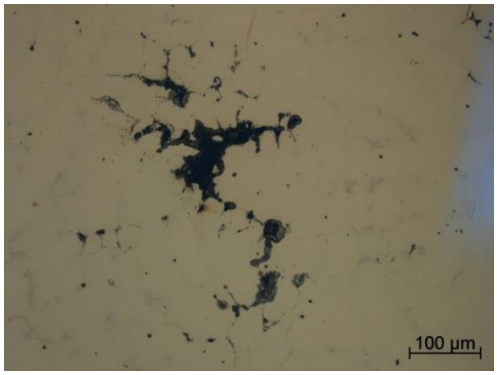

Figure 33. Optical image at 200X of the as received cast Co-Cr-Mo-C alloy exhibiting porosity

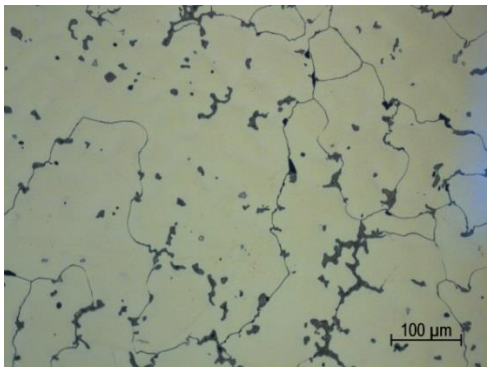

Figure 34. Optical image of the cast Co-Cr-Mo-C alloy microstructure taken at 200X exhibit grain size of approximate 150 µm.

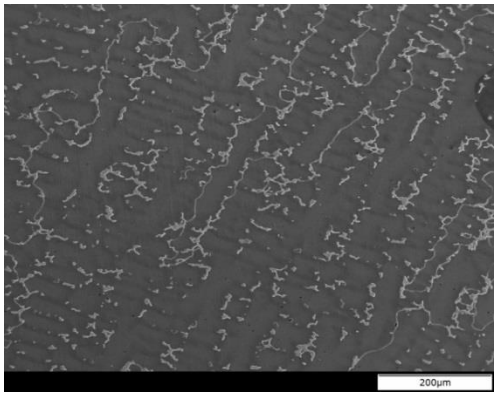

Figure 35. SEM image of cast Co-Cr-Mo alloy at 100X magnification

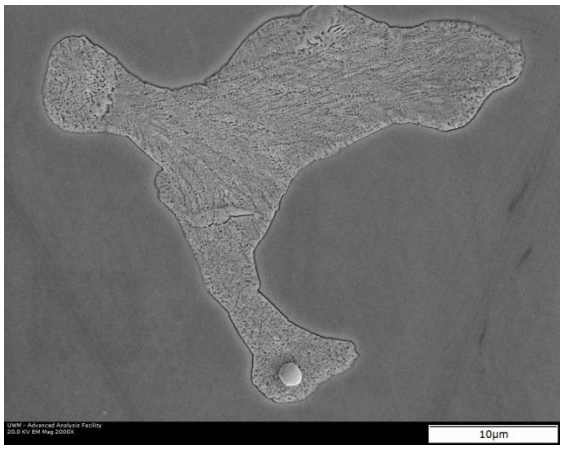

Figure 36. SEM image of alloy microstructure at 2kX magnification

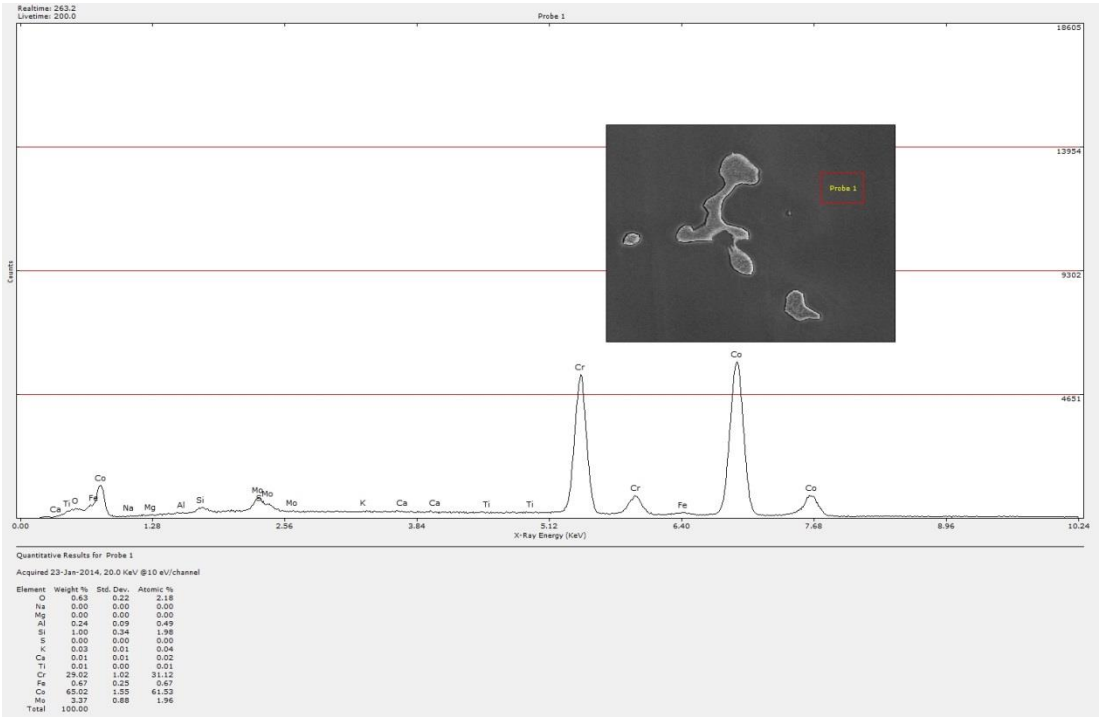

Figure 37. EDS analysis of the cast Co-Cr-Mo-C alloy matrix

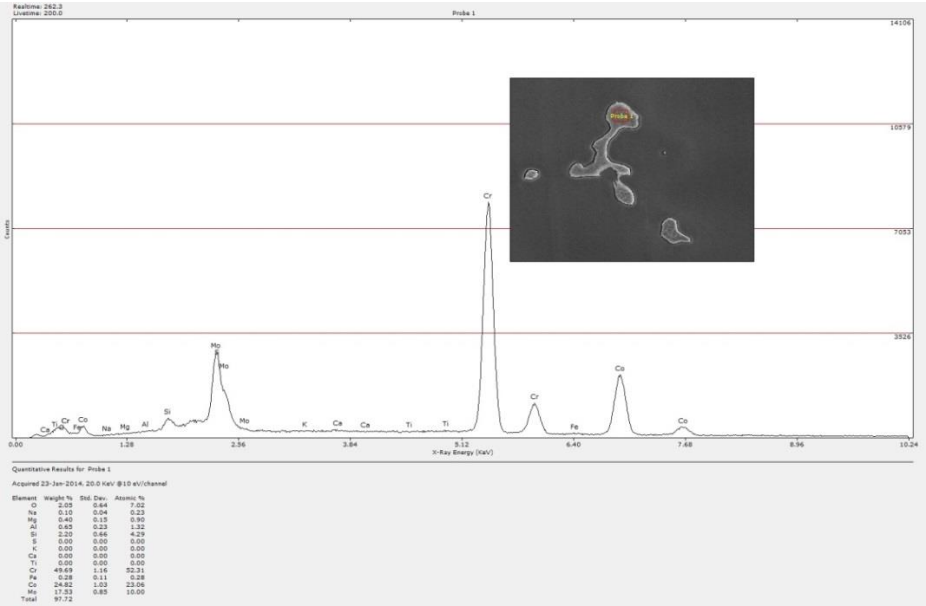

Figure 38. EDS analysis in the carbide precipitae (Co-Cr-Mo 23 C6)

In addition, little black spots found in the alloy microstructure, which were reported by Giacchi as inclusions [33]. EDS analysis confirms the presence of inclusions rich in Silicon found in the as cast matrix (Figure 40).

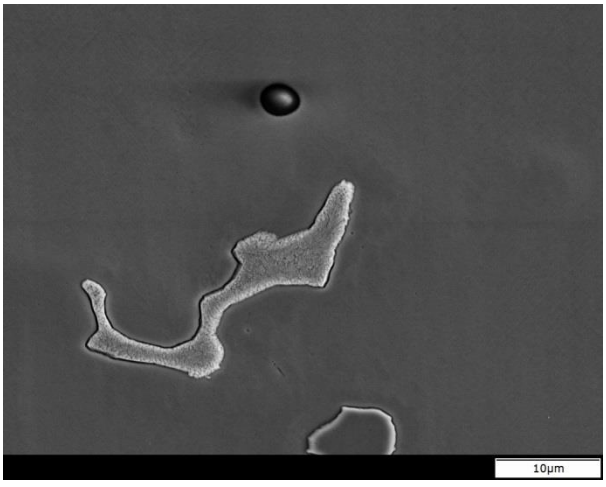

Figure 39. SEM image taken at 1500X confirms the appearance of inclusions inside the matrix alloy

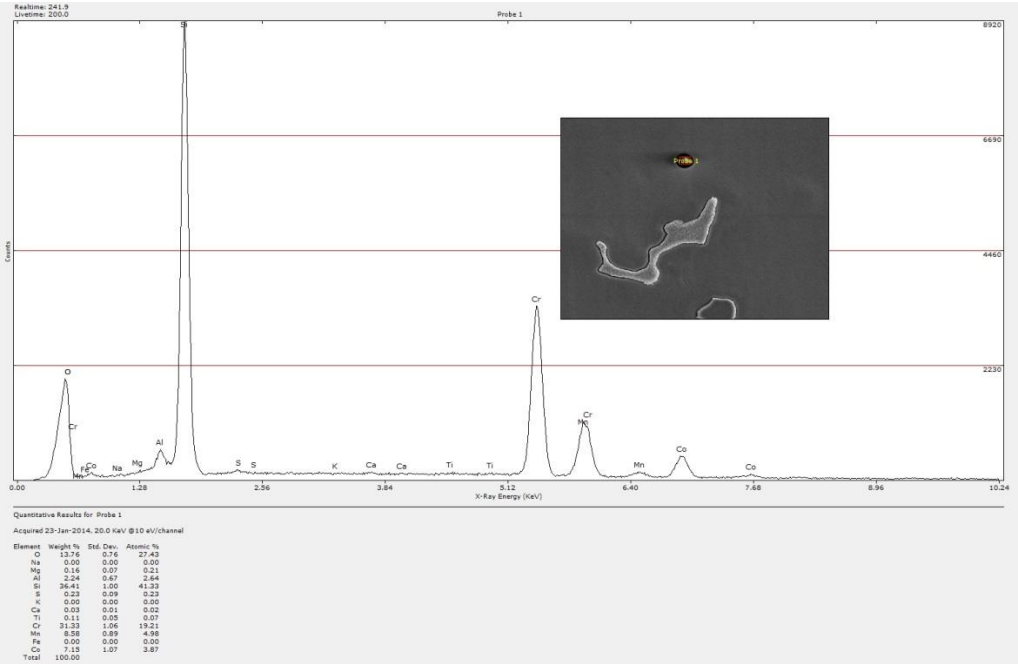

Figure 40. EDS analysis of the inclusion rich in Silicon

In cast Co-Cr-Mo-C alloys it is expected to find a dominant FCC phase in the alloy microstructure. The X-Ray analysis displays a large intensity peak at the 2θ angle of 50.5°. This pronounced peak corresponds to the crystal FCC phase in the alloy, and a small peak corresponding to the developed HCP phase is located at 2θ angle of 46.5° respectively.

Quantitative calculations of the developed HCP phase using Equation 13 displays 13% ε-martensite phase developed in the as cast microstructure. This result can be attributed to the small volumen fraction of HCP remained in the cast microstructure upon relative slow solidification [8].

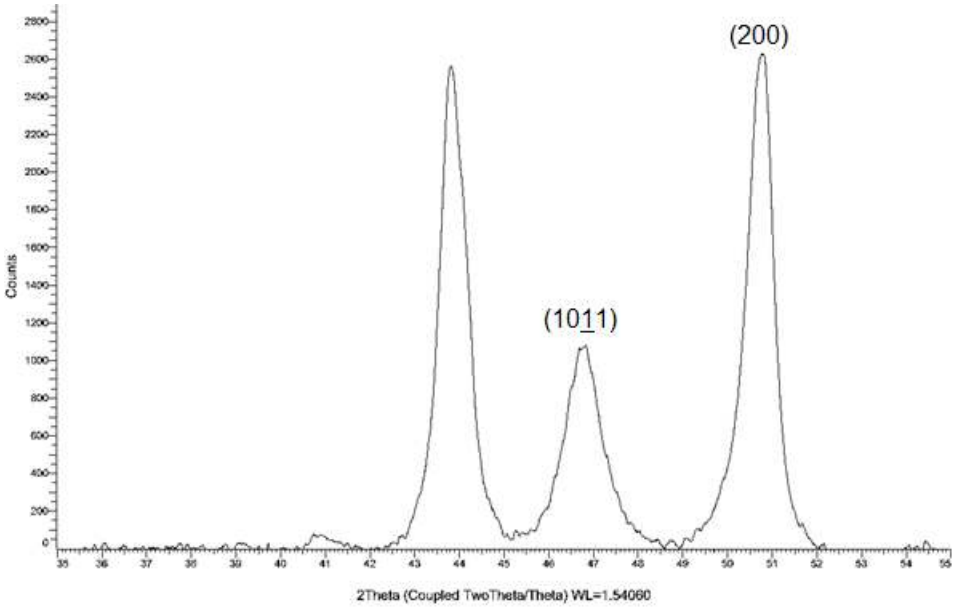

Figure 41. XRD patterns of the as cast Co-base alloy

$$\%HCP_{CAST} = \frac{[3.473u^2]}{[3.473u^2 + (1.5 * 15.17u^2)]} * 100$$

$$HCP_{CAST} = 13.24\ \%$$

4.1.2 Annealed Specimen

As mentioned before in the experimental section, the received annealed heat treated and surface modified using TIG welding Cobalt-base alloy specimens were delivered by the Amirkabir University of Technology in Tehran, Iran. An image of both as received specimens is shown in Figure 42.

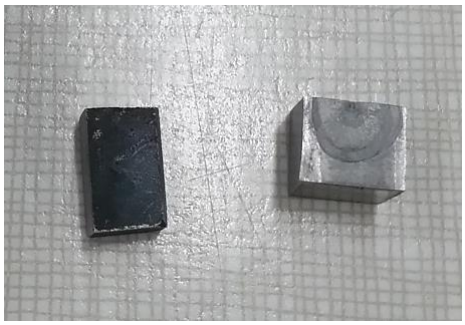

Figure 42. As received Solution annealed specimen (left). As received TIG melted specimen (right)

Solution heat treatment at 1230ºC promoted carbide dissolution in the alloy microstructure, given rise to increase ductility [34]. A fine distribution of carbides at the interdendritic regions was found in the microstructure with possible M23C6 carbide type formation along the grain boundaries of approximate 7 µm to 15 µm in size (see Figure 43).

EDS analysis displays Cr-rich carbides with Cr content of up to 53 wt%, and silicon rich inclusions (49 wt%) in the FCC-Cobalt matrix were found, similar to the as cast sample (see Figure 44 and 45). Apparently the Si-compounds remained stable during the solution annealing treatment.

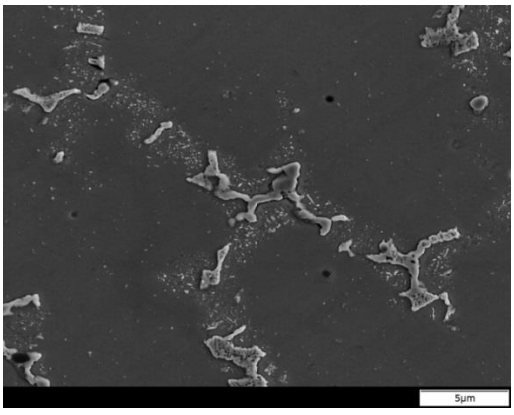

Figure 43. SEM image taken at 1500X of the annealed specimen exhibiting approximate 30 µm in grain size.

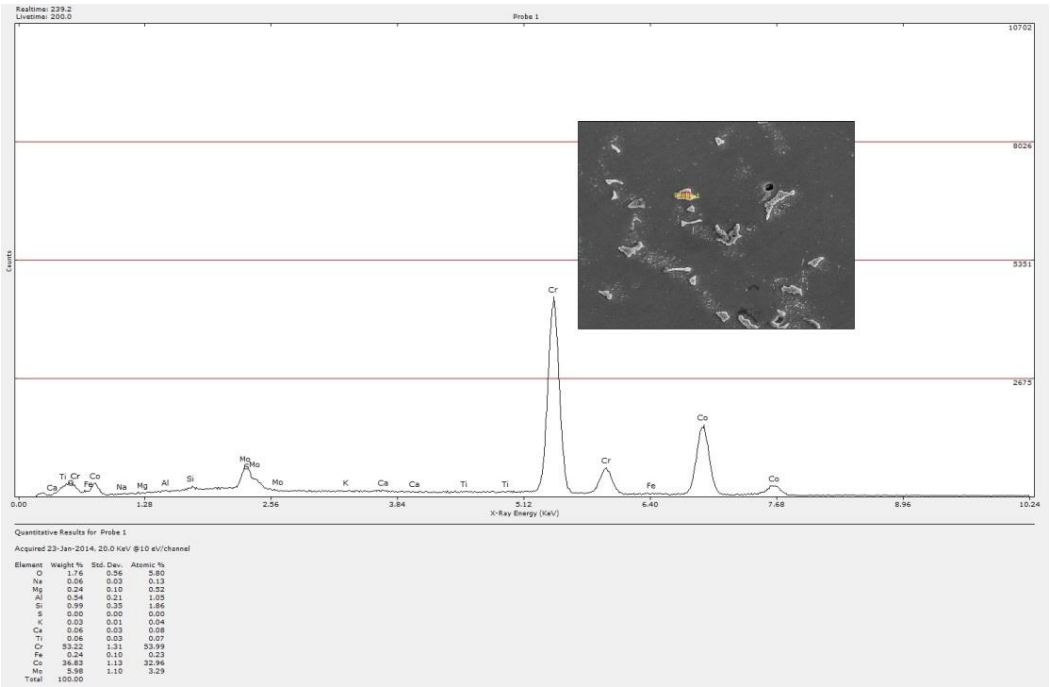

Figure 44. EDS analysis image of a possible carbide precipitate

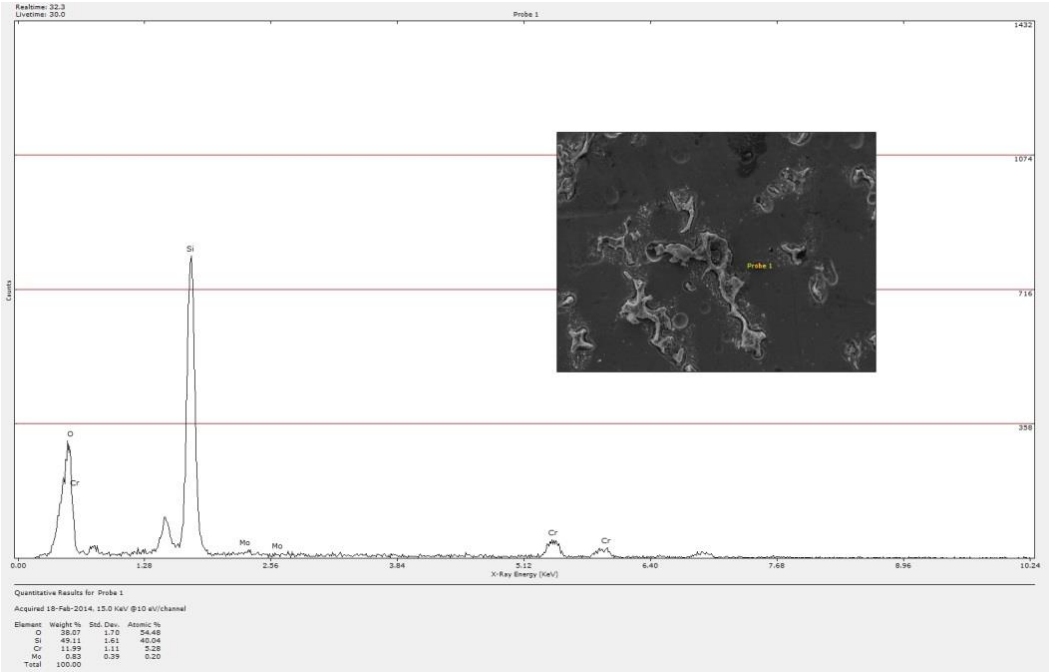

Figure 45. EDS analysis of an inclusion rich in Silicon

The amount of athermal transformation (HCP phase) after solution annealing at 1230°C was calculated quantitatively using the X-Ray diffraction patterns and the Sage and Guillaud method [31].

It was found that approximately 24% HCP phase has been formed after cooling from the solution annealing treatment at 1230^0C. Apparently, most of the metastable FCC phase was retained after quenching in water at room temperature. Also, intensity peaks demonstrate that heat treatment above 1150°C promotes ε-martensite phase after quenching at room temperature due to the FCC↔HCP kinetics of athermal transformation [35]. Furthermore, it has been reported that the increment of the HCP phase by athermal transformation is a function of the temperature used in solution annealing and the holding time [36].

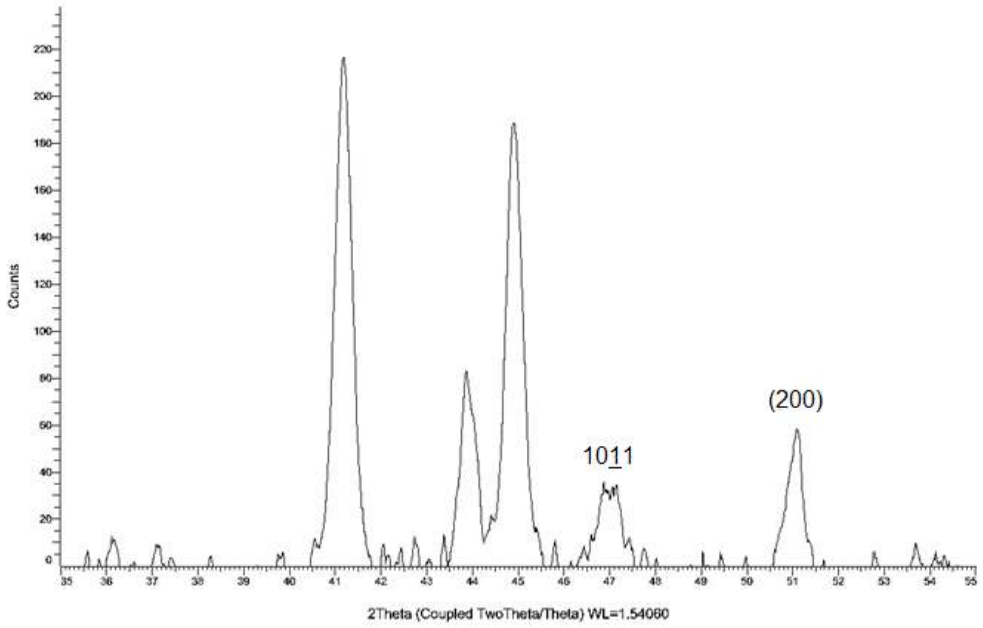

Figure 46. XRD patterns of the annealed Co-base alloy at 1230°C

$$\%HCP = \frac{[I_{(10\bar{1}1)_{HCP}}]}{[I_{(10\bar{1}1)_{HCP}} + (1.5 * I_{(200)_{FCC}})]} * 100$$

$$\%HCP_{Annealed} = \frac{[0.07251u^2]}{[0.07251u^2 + (1.5 * 0.1459u^2)]} * 100$$

$$HCP_{Annealed} = 24.89\ \%$$

4.1.3 TIG Surface Modified Specimen (TIGSM)

After solution annealing, the sample surface was cleaned and welded using TIG fusion welding process. Once the melt on the surface metal solidifies, the alloy microstructure rearranges itself into fine grains and dendritic regions. However, the difference in solidification rates promotes inhomogeneous dendrite distribution in the fusion zone as shown in Figure 47.

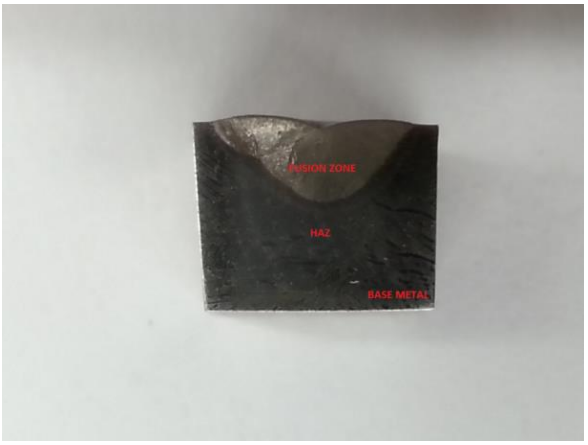

Figure 47. Stereo microscope image of the TIG surface modified specimen. The fusion zone, the heat affected zone, and the base metal can be identified once the alloy is electro-etched for 10sec.

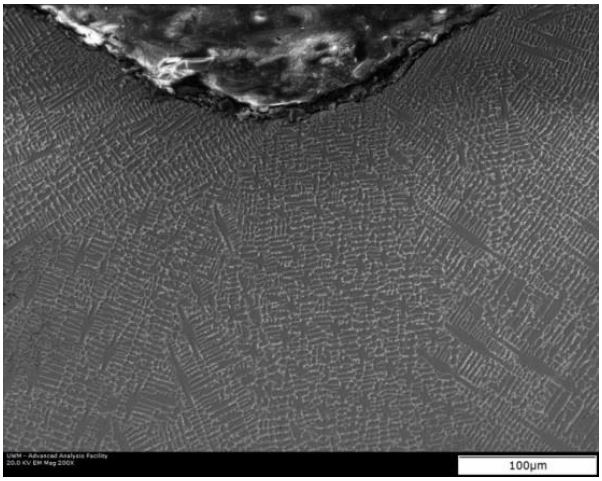

Figure 48. SEM image of the TIGSM specimen at 200X

The weld pool, close to the edge surface, contains uniform solute distribution with homogeneous dendritic and equiaxed regions in the microstructure as can be seen in Figure 49 and 50.

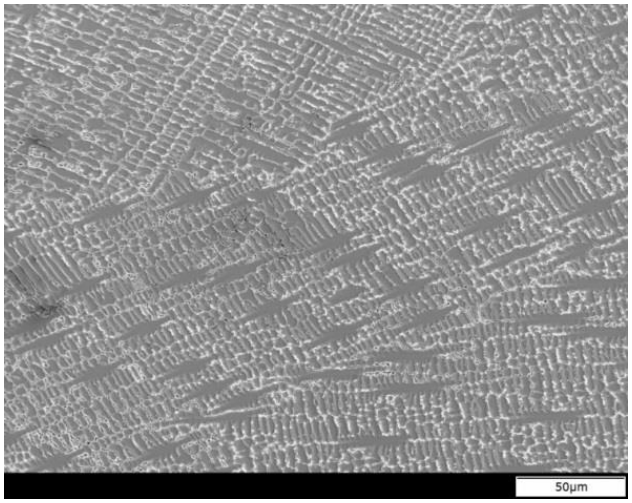

Figure 49. SEM image of the TIGSM specimen at 300X

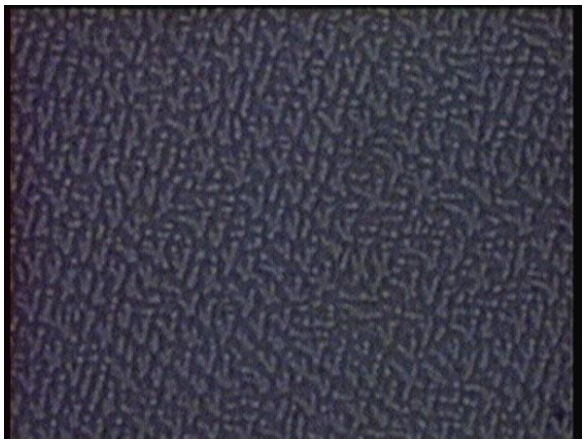

Figure 50 Optical microscope image of the weld pool at 400x in the TIGSM specimen

A reason for presenting a homogeneous microstructure close to the surface is the relative difference in solidification time as compared with the HAZ [21]. On the other hand, large dendritic regions with direction towards the fusion zone can be seen in Figure 51 and 52 as the HAZ is approached.

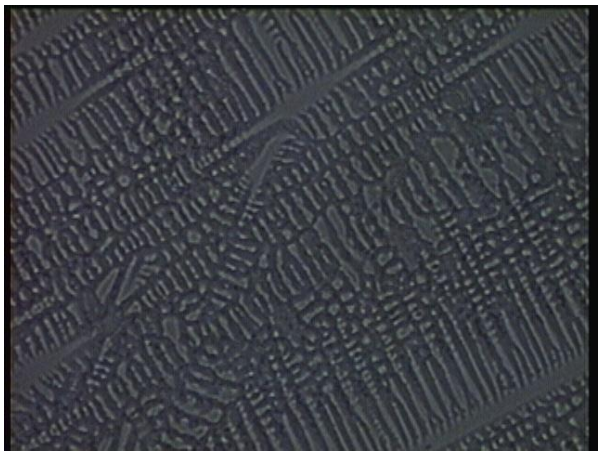

Figure 51. Optical microscope image of the weld pool at 400X in the TIGSM specimen

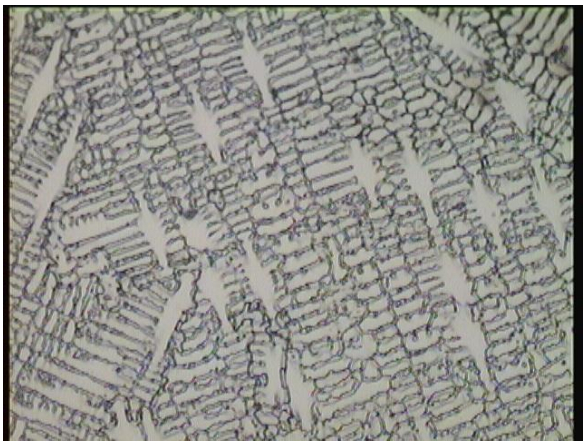

Figure 52. Optical microscope image of the weld pool at 400X in the TIGSM specimen

Columnar and equiaxed solidification modes can be distinguished in the weld area with grain refinement from 150 µm presented in the as cast alloy to approximate 10µm in the TIG surface modified specimen respectively.

Moreover, according to Figure 56, possible carbide precipitates along grain boundaries on a nanoscale size and Cr-rich were found in the solidified microstructure. Carbon precipitation in the fusion region may be associated with carbide type formation the same as type M23C6 found in the as cast alloy microstructure. Even though there are no confirmed results in literature of the type of carbides found in welded Co-Cr-Mo-C alloys, based on EDS results, the high cooling rates promoted by the TIG process may follow the same path in the precipitation of carbon. Similar results were found by Zangeneh and Lopez in surface melted Co-Cr-Mo-C alloys by TIG, where carbide precipitates in the form of CoCrMo23C6 were observed [37]. In addition, Silicon was identified by EDS analysis where it precipitated along the grain boundaries (see Figure 57).

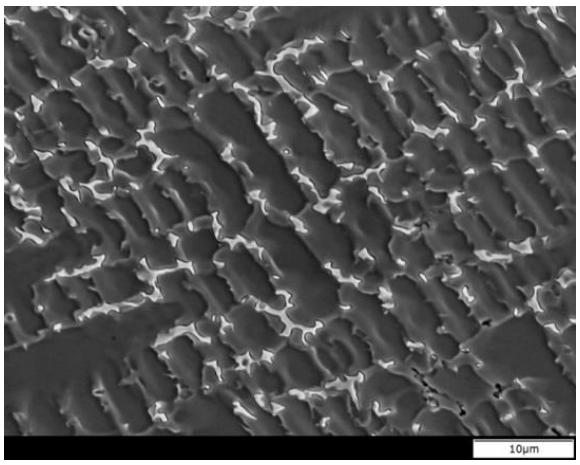

Figure 53. SEM image of weld pool at 1500X in the TIGSM specimen

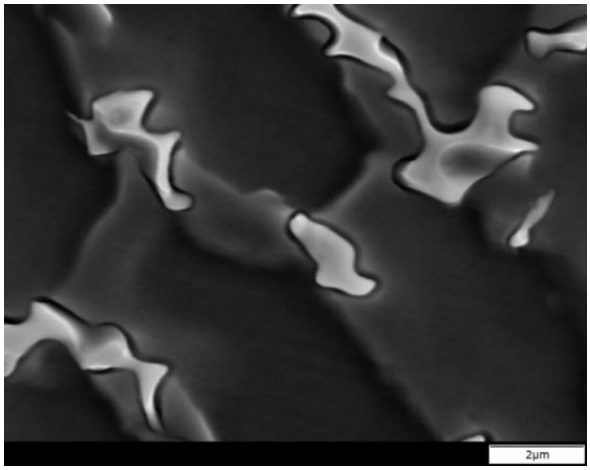

Figure 54. SEM image of the weld pool at 7kx in the TIGSM specimen describes an approximate grain and carbide precipitate sizes of 10µm and 5µm respectively.

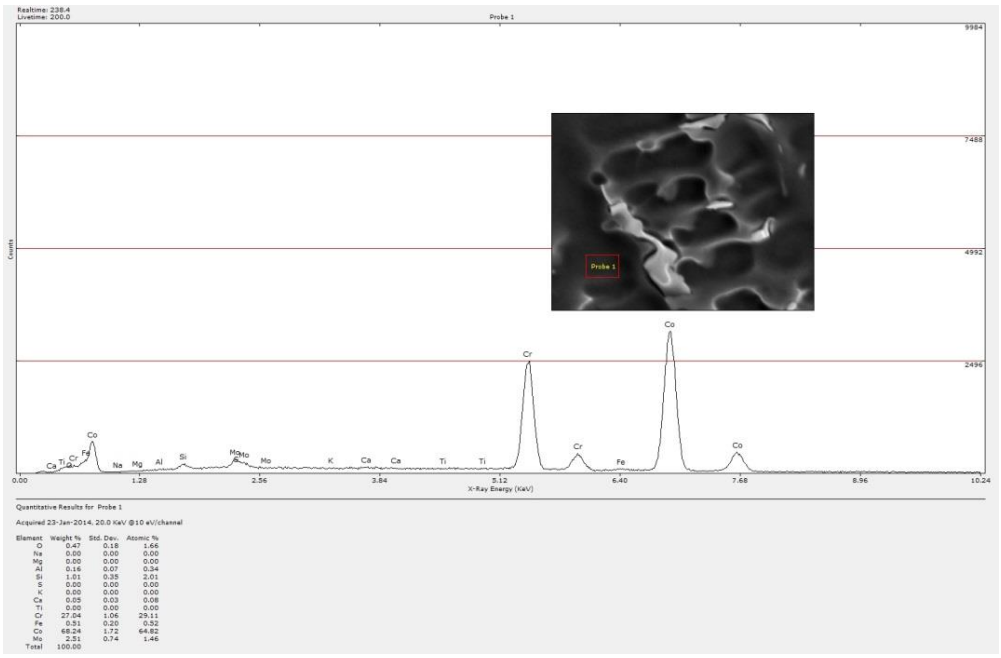

Figure 55. EDS analysis image of the grains inside the weld pool of the TIGSM specimen

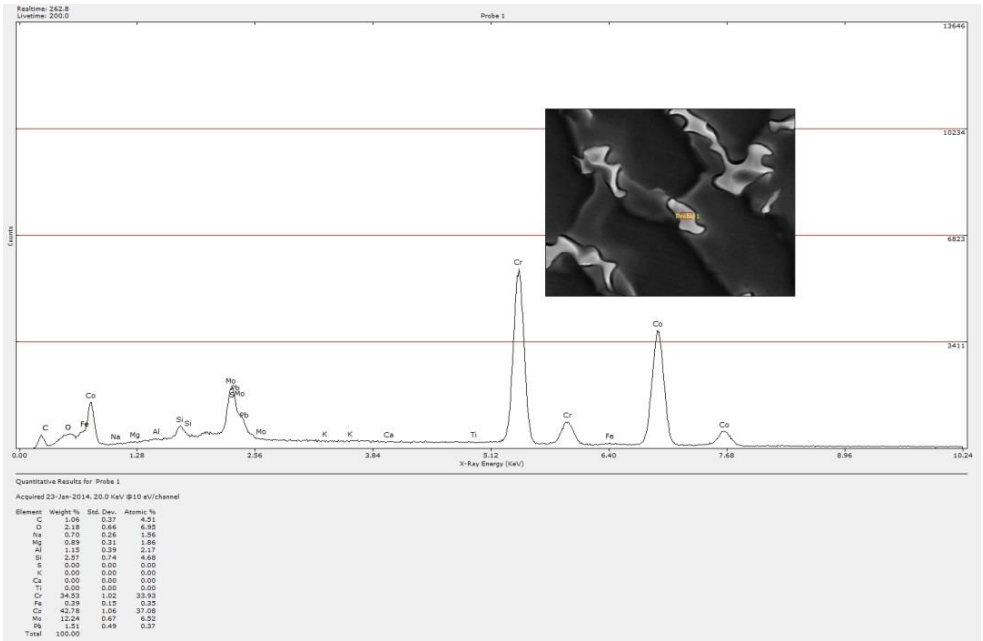

Figure 56. EDS analysis image of carbide precipitates found in the weld pool of the TIGSM specimen

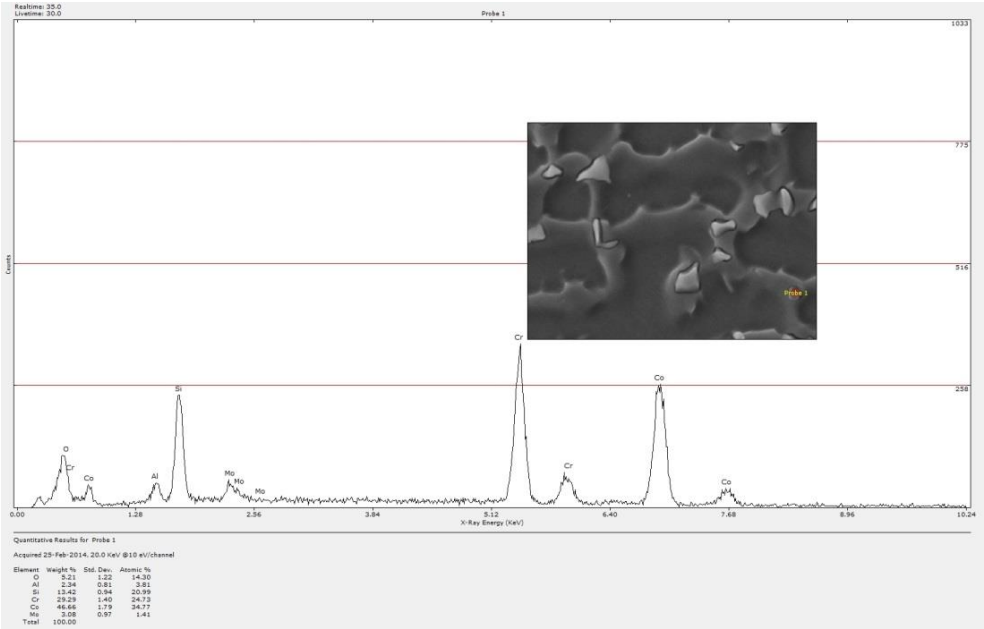

Figure 57. EDS analysis of the weld pool in the TIGSM specimen containing silicon inclusions along the grain boundaries

As the heat affected zone is approached, the solidified HAZ region presents a heterogeneous dendritic columnar solidification mode due to slow growth rate at the solid/liquid interface. As some coarse grains and interdendritic regions are noticed in the HAZ, the weld microstructure returns to its original form of the base metal microstructure.

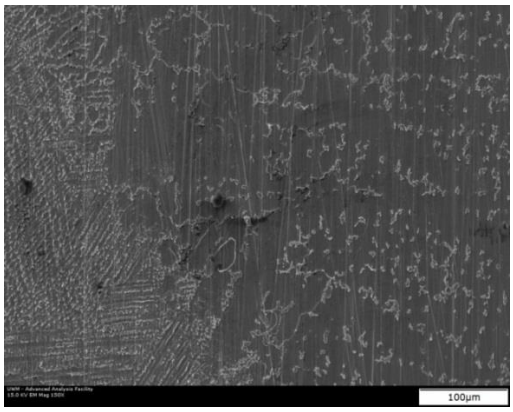

Figure 58. SEM image of the HAZ at 300X in the TIGSM specimen

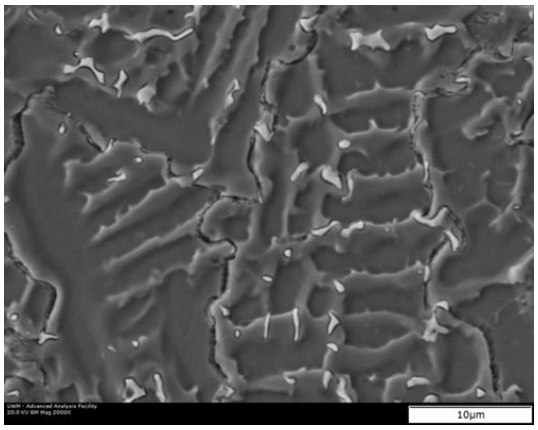

Figure 59. SEM image of the HAZ at 2kX in the TIGSM specimen

X-Ray diffraction was used to calculate the developed HCP phase in the weld region. The calculation of phase formation in the TIG treated alloy follows the same procedures as mentioned before for the as cast specimen. The TIG process promoted the development of partial ε-martensite HCP phase in the alloy microstructure (approximately 51%). The kinetics of transformation FCC↔HCP phase above 1100°C suggests that after quenching at room temperature from γ-FCC phase, HCP embryos will start developing and increasing as time and temperature is increased [38].

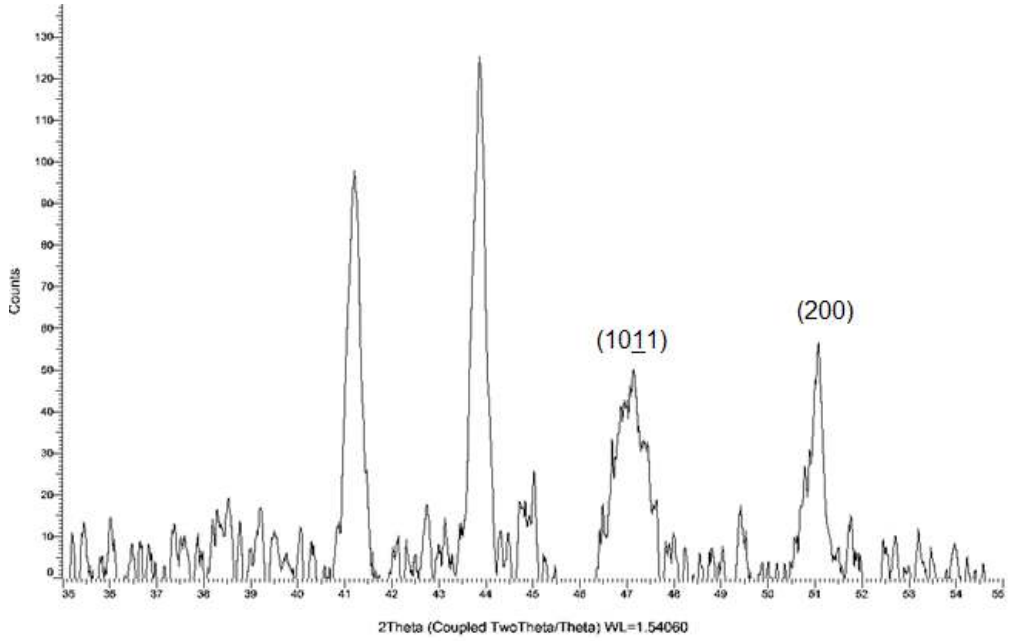

Figure 60. XRD patterns of the TIGSM specimen

$$\%HCP_{TIGSM} = \frac{[0.2018u^2]}{[0.2018 + (1.5 * 0.1255u^2)]} * 100$$

$$HCP_{TIGSM} = 51.74\ \%$$

4.1.4 Laser Surface Modified Specimen (LSM)

Figure 61 illustrates how Laser beam process was applied to promote local heat in the as cast Co-Cr-Mo-C alloy in order to calculate the developed ε-HCP phase and compare the results with the other specimens.

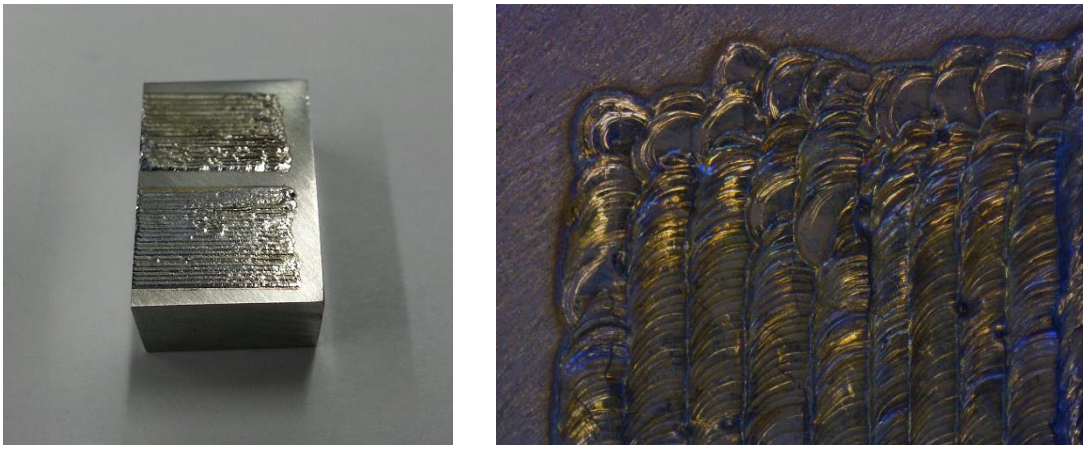

Figure 61. Image of the as received Co-Cr-Mo-C alloy. Laser surface modified specimen (left) and the laser weld beads profile taken in stereo microscope (right).

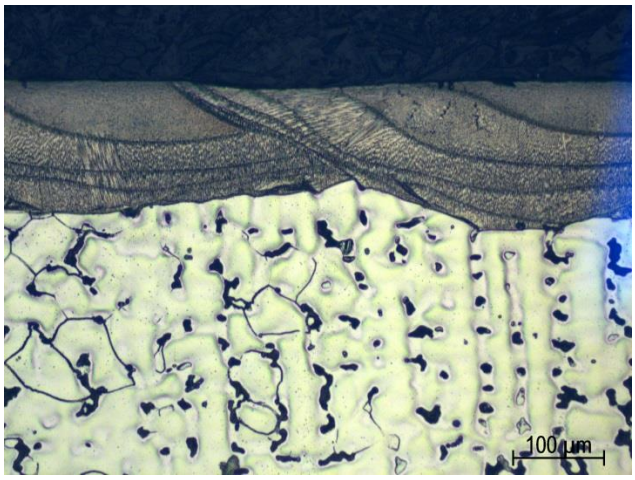

Figure 62. Optical microscope image of the laser weld beads taken at 200x

After promoting melting on the surface alloy by the bombardment of electron beams, it was found that fine homogeneous cellular solidification mode (see Figure 63) takes place in the microstructure with ultrafine grain size of approximately 2µm as it is shown in Figure 66.

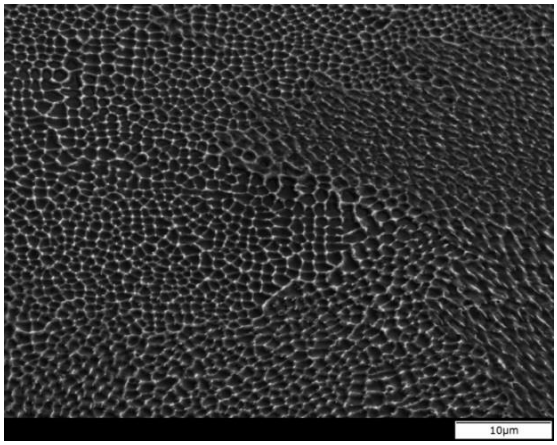

Figure 63. SEM image of the weld pool taken at 1500X for the LSM specimen

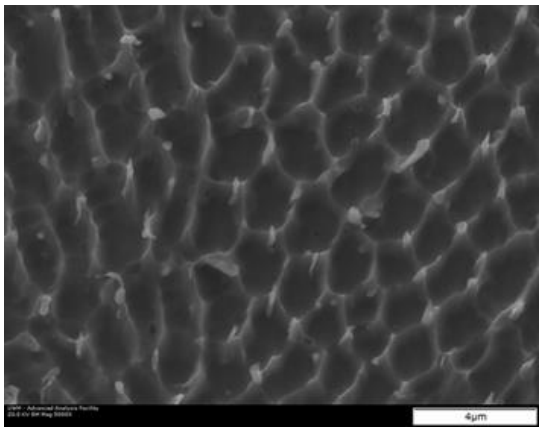

Figure 64. SEM image of the weld pool taken at 5kX for the LSM specimen

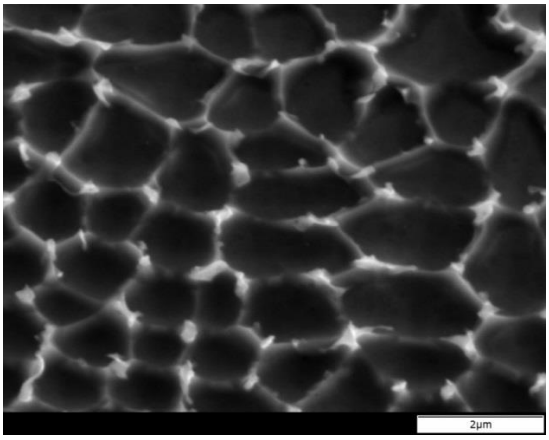

Figure 65. SEM image of the weld pool taken at 10kX for the LSM specimen

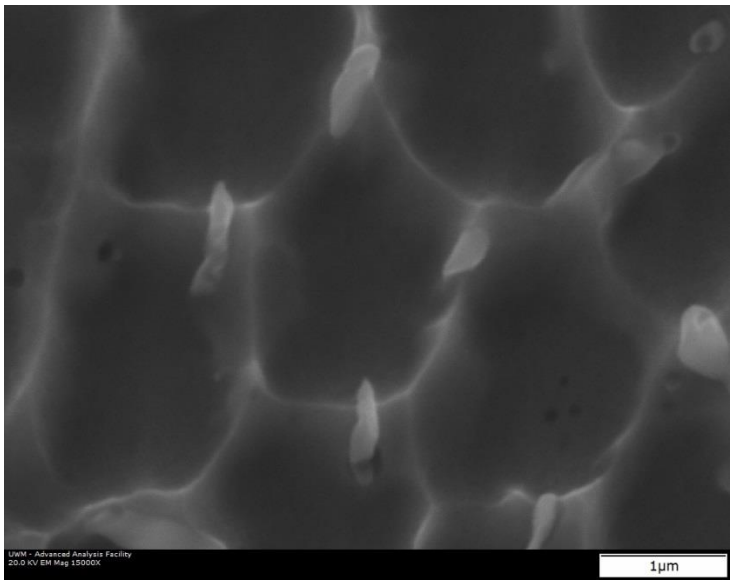

Figure 66. SEM image of the weld pool taken at 15kX for the LSM specimen

Figures 64 and 65 describe how the possible carbides precipitate at the grain boundaries with a compact re-arrangement of homogeneous cellular regions containing ultrafine grains.

EDS analysis refers to possible $(\mathrm{CoCrMo})_{23}C_6$ carbide type precipitation in the dendritic region similar to the thermally surface modified specimen by TIG process. The only difference between both specimens is the carbide size formation at the grain boundaries. The LSM specimen is $\frac{1}{5}$ smaller in size compared to the TIGSM specimen (less than 1µm in Laser treated and 5µm in TIG process), which may lead to improvement in corrosion and wear resistance.

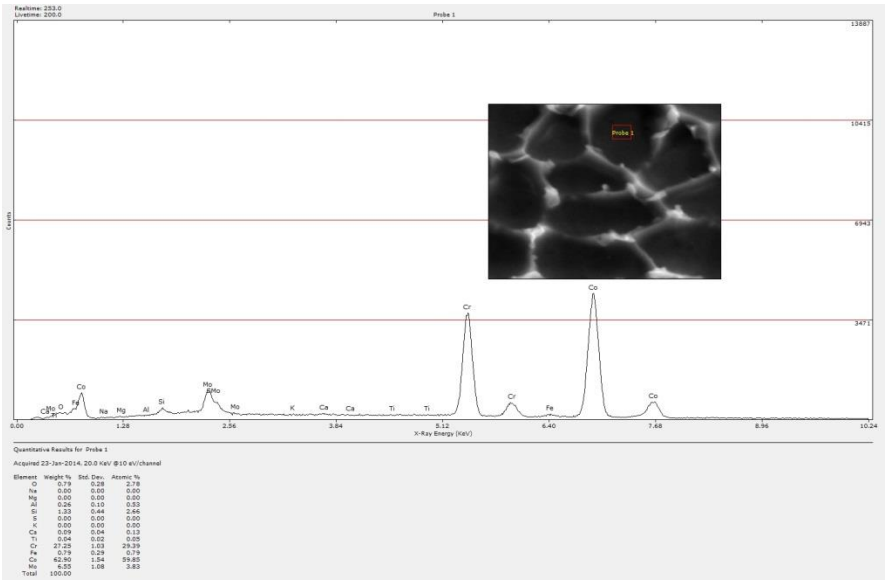

Figure 67. EDS analysis image of grains found in the weld pool of the LSM specimen

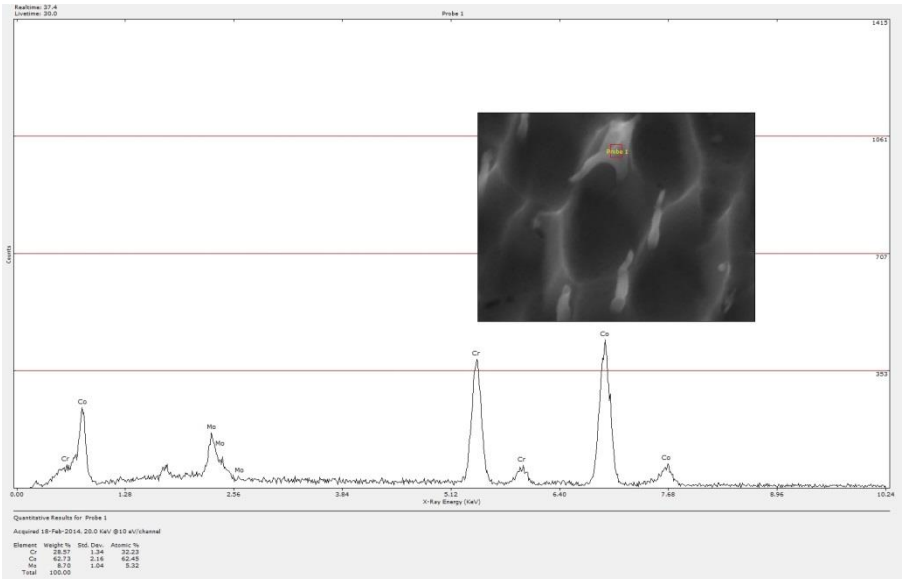

Figure 68. EDS analysis image of possible carbide precipitates found in the weld pool of the LSM specimen

Laser Beam Welding has the advantage of providing to the weld low heat input, good penetration, and small heat affected zone. Figure 69 describes the solidification at the interface between the weld, HAZ, and the base metal. The HAZ region is very thin, which is a characteristic in Laser welding processes, and it is difficult to identify. However, an SEM image (Figure 70) shows how the interdendritic and fine dendritic areas become mixed at the solid/liquid interface and the dendrites follow the direction of the liquid.

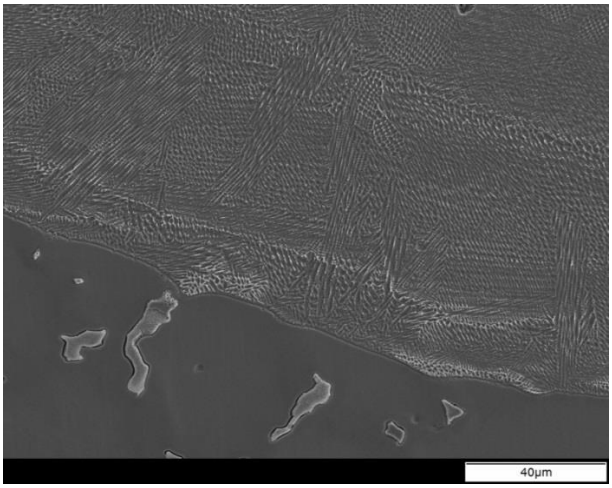

Figure 69. SEM image of the weld pool taken at 500X for the LSM specimen

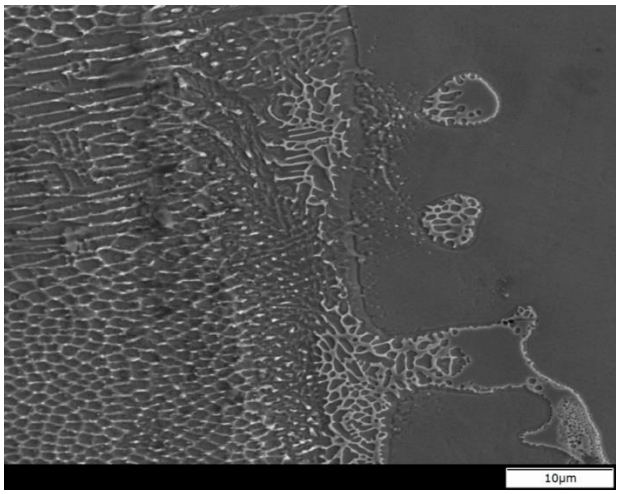

Figure 70. SEM image of the weld pool taken at 500X for the LSM specimen

Even though most areas inside the weld pool exhibit a refined microstructure, some layers close to the HAZ and the base metal regions show heterogeneous microstructures with some columnar dendrites on the bottom and equiaxed grains (Figure 72). Once the heat input creates the fusion zone, a molten layer extends throughout the alloy surface and will solidify depending on its cooling time. In other words, the bottom layer receives relative less time to solidify compared to the top layer on the alloy surface, which may lead to a change in solute redistribution. However, EDS analysis describes no difference of solute in the entire weld.

Figure 71. SEM image of the weld pool taken at 500X for the LSM specimen

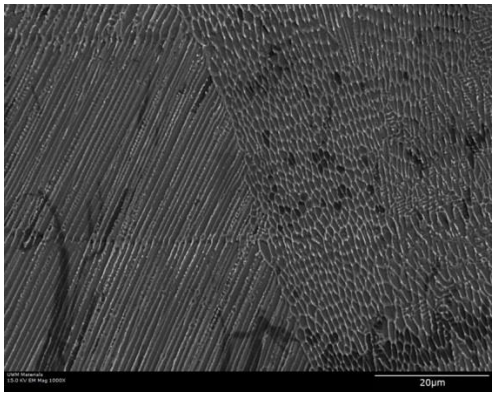

Figure 72. SEM image of the weld pool taken at 1500X for the LSM specimen

X-Ray diffraction analysis was performed on the alloy surface in order to calculate the amount of athermal HCP phase developed in the LSM specimen. The intensity peaks at the angles of interest reveal a formation of 2% ε-martensitic HCP in the alloy microstructure.

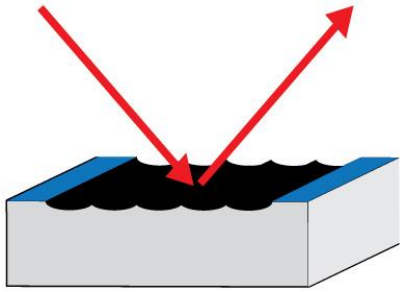

Figure 73. X-Ray diffraction scheme for the LSM specimen

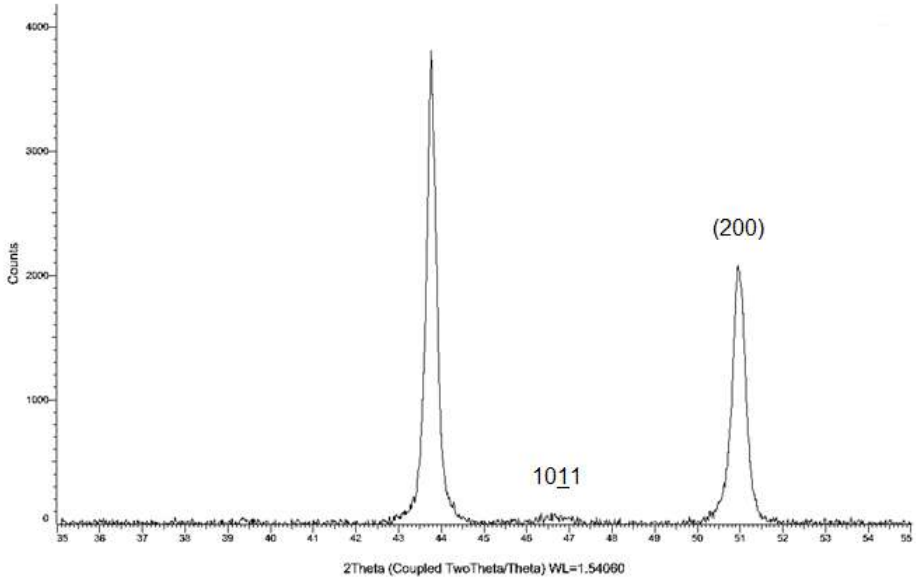

Figure 74. XRD patterns of the LSM specimen

$$\%HCP_{LSM} = \frac{[0.1778u^2]}{[0.1778u^2 + (1.5 * 3.869u^2)]} * 100$$

$$HCP_{LSM} = 2.97\ \%$$

4.2 Micro-hardness

Micro-hardness readings were taken in the as cast alloy with an average reading of 353HV (Table 2), which meets the ASTM F-75 standard specifications [30].

	Micro-hardness (HV500)					
	R1	R2	R3	R4	R5	Average
As Cast specimen	346.9	361.4	357.2	352.8	348.1	353.28

Table 2. Micro-hardness reading of the as cast specimen

After the as cast alloy was taken into solution annealing followed by rapid quench in water at room temperature, it exhibited a light increment in micro-hardness values (Table 3). The reason for the increment in hardness may be related to phase transformation in the alloy as demonstrated by X-Ray analysis.

The annealing temperature of 1230°C introduced in the as cast α-FCC alloy promotes thermal activation in the predominant FCC crystal structure. The HCP embryos will start the athermal transformation due to the change in free energy, which causes faults in the stacking sequence where the theory of Shockley partial dislocations governs the FCC↔HCP transformation [15] [39].

	Micro-hardness (HV500)					
	R1	R2	R3	R4	R5	Average
Anneal specimen	386.4	391.5	376.4	371.9	384.5	382.14

Table 3. Micro-hardness reading of the annealed specimen

The micro-hardness profile in the surface melted region for the TIG processing is shown in Figure 75, and the values for both TIG and Laser surface melting were plotted in Table 4 and 5. The highest micro-hardness value was obtained in the Laser melted pool (461.3HV) and for the TIG melted surface was nearly 43 points lower (418HV).

	Location from edge surface	Micro-hardness HV 500
ASTM F-75 TIGSM	0.005	418.0
	0.010	392.6
	0.020	384.6
	0.025	405.8
	0.040	417.1
	0.070	397.4
	0.100	399.4
	0.140	392.6
	0.160	387.8

Table 4. Microhardness values for the TIGSM specimen

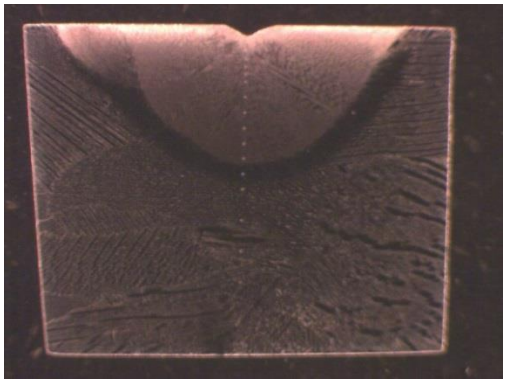

Figure 75. Stereo microscope image of the micro-hardness profile in the TIGSM specimen

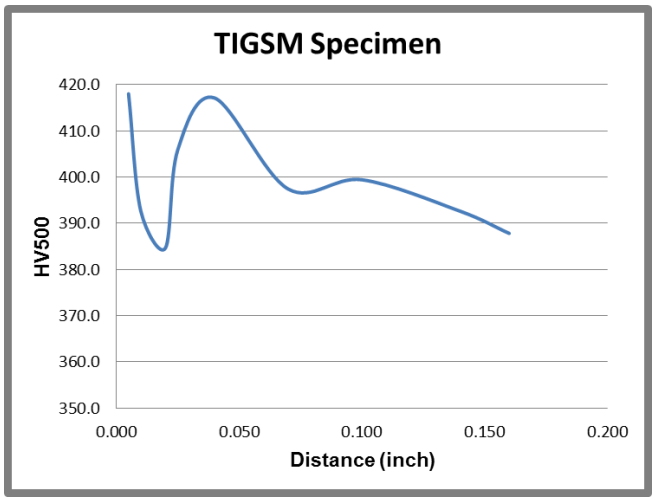

Figure 76. Vickers Micro-hardness chart taken from edge surface with direction towards the base metal in the TIGSM specimen

LSM Specimen	Micro-hardness (HV500)					
	R1	R2	R3	R4	R5	Average
	456.5	468.2	461.3	451.9	468.6	461.3

Table 5. Micro-hardness reading of the LSM specimen

One of the reasons for lower micro-hardness values in the alloy melted by TIG process could be attributed to the less homogeneous interdendritic areas found in the microstructure. The homogeneous carbide distribution and cellular regions found in the LSM specimen may cause to obtain consistent and higher hardness values. However, micro-hardness values for the TIGSM specimen increase in a certain distance from the surface. This reason could confirm that homogeneous fine microstructures in Co-Cr-Mo-C alloys lead to higher hardness values.

Another reason for low values in micro-hardness is because the amount of athermal HCP phase formed in the TIG melted region. The LSM exhibits less ε-martensite phase transformation than the TIGSM specimen.

Furthermore, according to tables 2 and 3, the micro-hardness for the annealed specimen is 382HV and for the as cast specimen is 353HV, which implies that highest hardness values can be obtained when the alloy microstructure is refined giving rise to less coarse grain and carbide sizes .

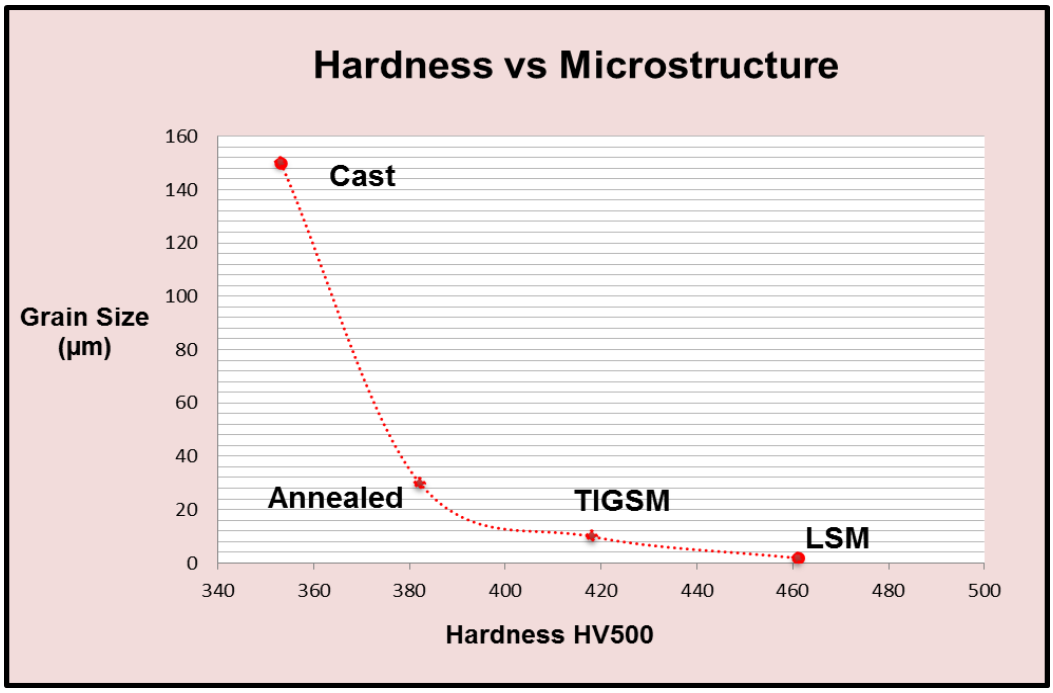

Figure 77. Relationship between grain size for each alloy condition and their respective micro-hardness reading

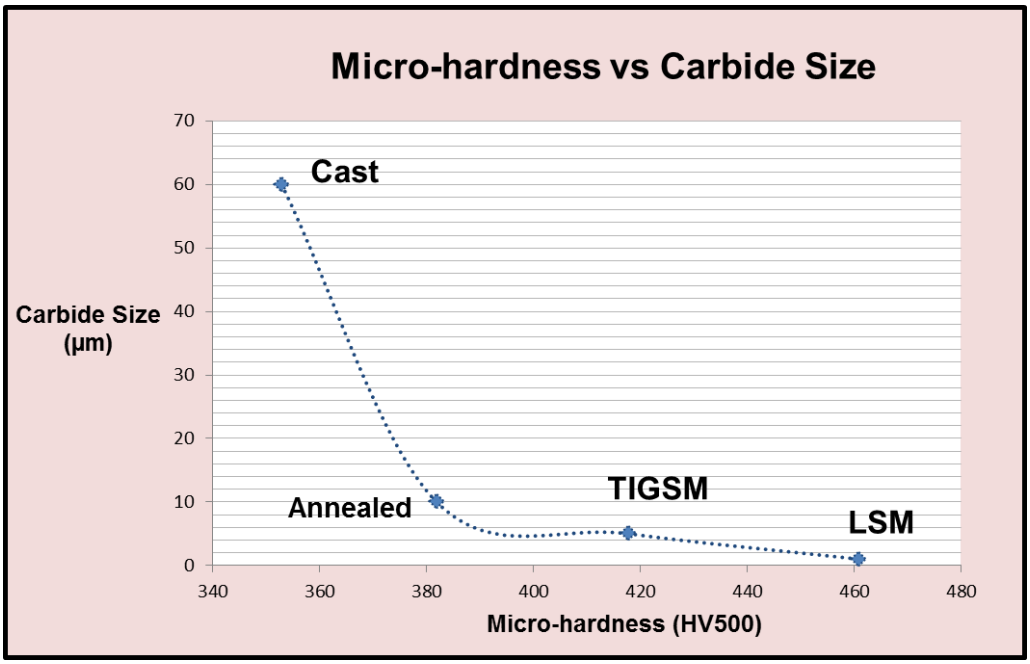

Figure 78. Relationship between carbide size for each alloy condition and their respective micro-hardness reading

4.3 Corrosion

The driving force for corrosion resistance in Co-Cr-Mo-C alloys is the passivation of Chromium in the metal alloy surface [40]. In the active region, Cr ions react with oxidants to create an oxidized passive film (Chromium oxide Cr_2O_3). In order to break the oxidized passive film, Cr_2O_3 will react with Hydrogen to re-activate anodic dissolution on the alloy surface. Then the transpassive film is breakdown by the oxidation of Chromium oxide.

$2Cr + 3H_2O \rightarrow Cr_2O_3 + 6H^+ + 6e^-$ passive film formation

$Cr_2O_3 + 6H^+ \rightarrow 2Cr^{3+} + 3H_2O$ passive film dissolution

$Cr_2O_3 + 5H_2O + 6e^- \rightarrow 2{CrO_4}^{2-} + 10H^+$ transpassive film dissolution

It was found that the corrosion resistance in the as cast Co-Cr-Mo-C alloy under Ringer solution (pH=7) is 1.712 µm/year, which confirms the corrosion resistance rate of 1.65 µm/year to 2.59 µm/year for Co-Cr-Mo alloys reported by Hsu and Wen-Wei [41]. In this investigation, the observed highest corrosion resistance value was found for the specimen treated by Laser (435 nm/year). On the other hand, the TIG treated specimen exhibits the least corrosion resistance value (15.55 µm/year).

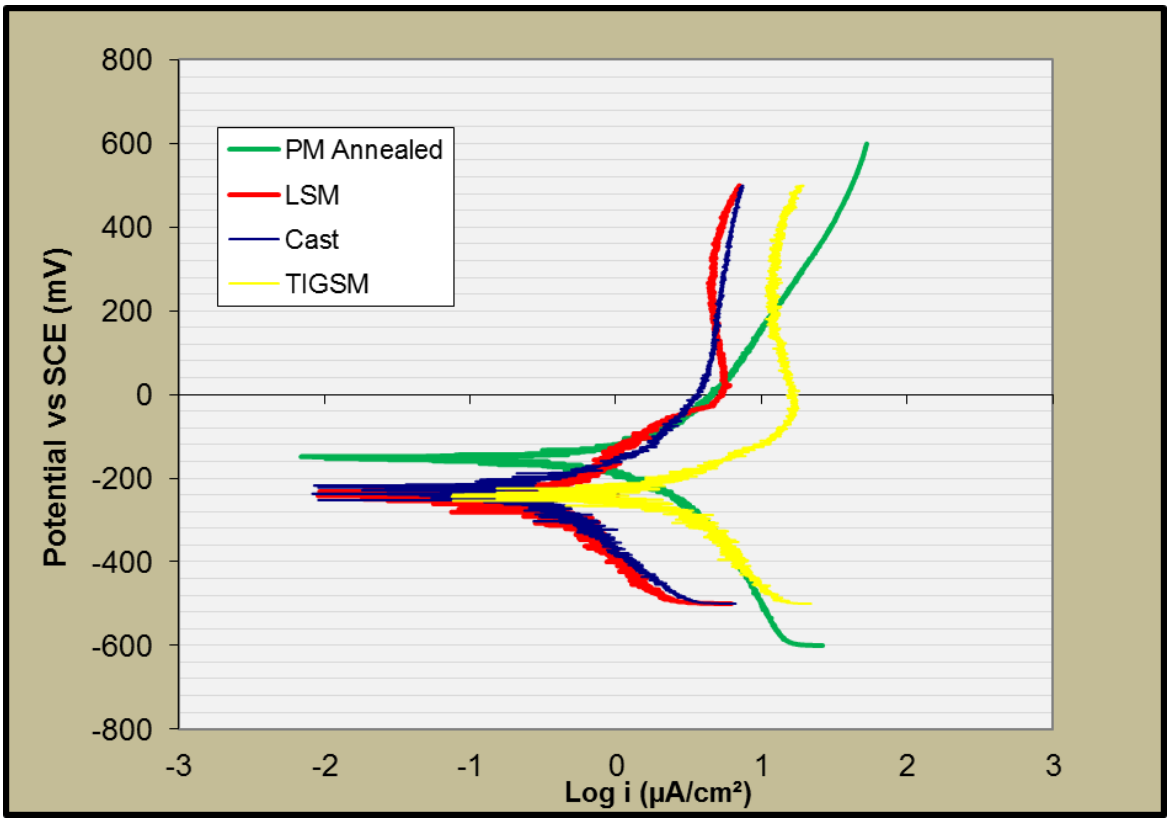

Figure 79. Corrosion potentiodynamic curves for each alloy condition and a reference sample

Material	E (mV)	Icorr (µA/cm2)	βa (mV)	βc (mV)	Coefficient	Corrosion Rate (µm/year)
As cast specimen	-226.8	0.1673	101.3	-149.9	0.9805	1.712
PM Annealed	-154.4	0.5649	127.4	-138.2	0.9791	8.363
TIGSM specimen	-243.5	1.0505	117.3	-116.8	0.9807	15.55
LSM specimen	-210.9	0.0425644	34.1	-91.5	0.9751	0.435

Table 6. Corrosion rate for each alloy condition calculated by the Tafel extrapolation method

In Figure 79 the anodic and cathodic polarization curves obtained for each alloy condition and the reference sample in Ringer solution can be well distinguished.

The reference sample is a Co-Cr-Mo-C alloy and contains the same heat treatment parameters and chemical composition as the annealed sample. However, the reference sample is processed by powder metallurgy and it is used in this investigation for corrosion comparison only.

The passive zone for both the as cast and LSM specimens is formed at the current density value of 0.7µA/cm2 (logarithm scale) and at the corrosion potential of -10mV respectively. However, the Laser melted alloy anodic curve exhibits a little deviation in current density to finally reach stability at 0.5 µA/cm2 and 200mV.

In contrast, the passive film of the anodic polarization curve for the TIGSM is shifted at higher current intensity values (above 1 µA/cm2). In other words, the

corrosion resistance decreases for the TIG treated alloy as the current density increases.

Even though the TIG treated alloy displays similar corrosion potential values as those observed in the other alloy conditions (-10 mV to 500mV), the formation of the passive zone for the TIGSM specimen becomes critical as its corrosion resistance decreases (see Table 6).

Process	Grain Size (µm)	Carbide Size (µm)	Micro-hardness (HV500)	HCP (wt%)	Corrosion Rate (µm/year)
Cast	150	60	353	13	1.7
Annealed	30	10	382	24	
TIGSM	10	5	418	51	15.5
LSM	2	1	461	2	0.4

Table 6. A summary of all values found on this investigation

The presence of low amount of ε-martensite phase in the microstructure (2% in LSM and 13% in the as cast) for both alloy conditions may have given rise to the passive zone caused at shift in potential values (from -10 mV to 500 mV) while the current density remains constant at 0.7 µA/cm2.

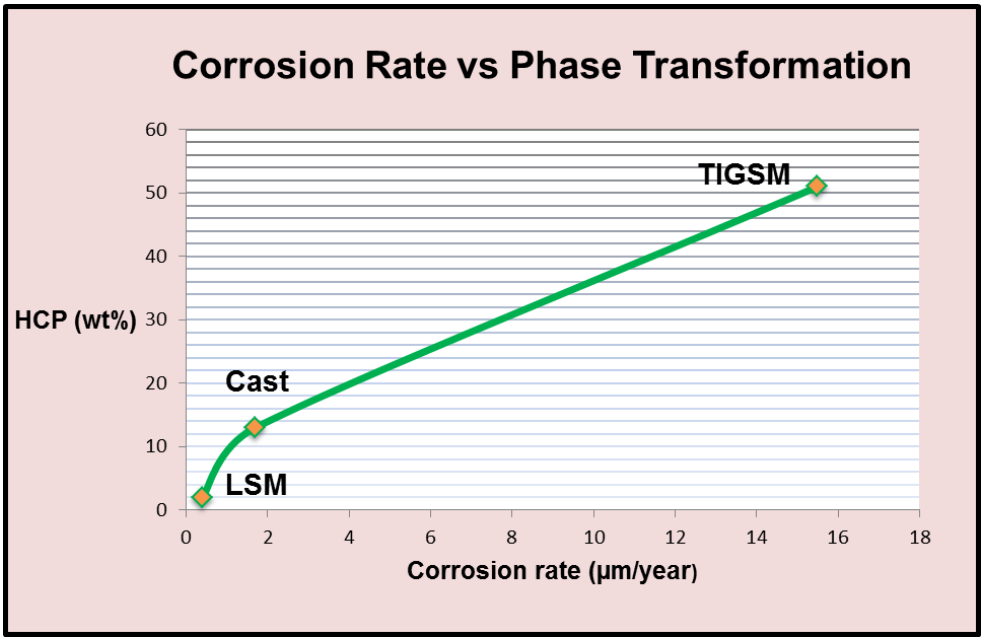

Figure 80. Corrosion resistance for each alloy condition according to the HCP phase developed in the microstructure.

According to Figure 80, the corrosion rate for each alloy condition increases as the developed HCP-phase in the microstructure increases as well. Therefore, it could be considered that the corrosion resistance of Co-Cr-Mo-C alloys is attributed to the development of ε-martensite in the alloy microstructure.

CHAPTER 5. CONCLUSION

In this work Cast Cobalt-Chromium-Molybdenum-Carbon alloys were investigated. Athermal martensitic transformations were induced to the cast alloy to understand the thermal effects on its microstructure and properties.

Four specimens were investigated: the as received cast alloy, a solution annealed specimen, TIG and Laser melted surfaces. The last three alloy specimens were physically modified by inducing annealing heat treatment and fusion welding processes in order to promote athermal transformation in the alloy microstructure.

The characterization of the microstructure was performed using metallography and microscopy techniques. The developed ε-martensite phase was calculated using X-Ray diffraction patterns. Corrosion test in Ringer solution was carried out to build a relationship between the developed ε-martensite and the corrosion rate in the alloy. The present investigation findings are summarized as follows:

1. The as cast Co-Cr-Mo-C alloy exhibits casting defects, such as porosity, coarse interdendritic morphology with an approximate grain size of 150 µm, coarse carbide precipitates type $(CoCrMo)_{23}C_6$, and inclusions rich in Silicon.
2. Solution annealing heat treatment at 1230°C promotes finer interdendritic microstructure (30 µm grain size and 10 µm carbide precipitation size)

3. Grain refinement from 150µm to 2µm in size can be achieved by surface modification using TIG and Laser processes. The precipitation of possible carbides occurs along the grain boundaries. However, it was found in the LSM specimen there is a mixed with cellular and columnar casting structure.
4. The amount of athermal martensite (HCP phase) was calculated for each alloy condition. The lowest volume percent of HCP phase developed in Co-Cr-Mo-C alloy microstructure corresponds to the LSM specimen (2%) followed by 13% in the as cast, 24% in the annealed, and 51% in the TIGSM specimen.
5. Vickers micro-hardness test were performed on each investigated specimen. The fine microstructure developed in the alloy, upon thermal gradients were induced, reveals a straight relationship with the obtained hardness values. As the grain size and carbide precipitates refine in the alloy microstructure, hardness readings increase reaching a maximum point of 461.3 HV found for the Laser processed surface. On the other hand, the lowest hardness value was found in the as cast condition due to coarse grains and carbide precipitates exhibited by this alloy.
6. The corrosion resistance in the alloy increases according to the volume fraction of the ε-martensite phase. The TIG process promoted the largest HCP volume percent value by inducing athermal transformation reaction FCC↔HCP. Therefore the corrosion rate increased significantly from 0.4 μm/year found in the LSM to 15.5 μm/year in TIGSM specimen.

REFERENCES

[1] Moore AT, Böhlman HR. The classic. Metal hip joint. A case report. By Austin T Moore and Harold R Bohlman. 1943. Clin Orthop. 1983. Jul, pp. 3–6.

[2] "Historical Perspective of Metallic Implants." NACE Resource Center. Apr.2014.http://events.nace.org/library/corrosion/Implants/Historical.asp>.

[3] "Journal of the American Academy of Othopaedic Surgeon." 16. (July 2008): n. page. Web.

[4] Lee, Sang-Hak, et al. "Effect of carbon addition on microstructure and mechanical properties of a wrought Co-Cr-Mo implant alloy." Materials Transactions-JIM 47.2 (2006): 287-290

[5] Brooks, C.R., Heat treatment, structure, and properties of nonferrous alloys., inMetals park. 1982: Ohio American Society for Metals. p. 229.

[6] R. Adams and C. Altstetter: Trans. TMS-AIME, 1968, vol. 242, pp. 139–3.

[7] T.B. assalski, H. Okamoto, P.R. Subramanian, and L. Kacprzak, Ed., Binary Alloy Phase Diagrams, Vol 2, 2nd ed., ASM International,1990, p 1214–1215.

[8] Hull, Derek, and David J. Bacon. Introduction to dislocations. Vol. 257. Oxford: Pergamon Press, 1984.

[9] C.T. Sims and W.C. Hagel, Ed., The Superalloys, John Wiley & Sons, 1972, p 145–174

[10] F. Sebilleau and H Bibring; “The allotropic transformation of cobalt”, Rev. Met. 1642, pp. 209-217, (1995)

[11] Ramírez LE, Castro M, Méndez M, Lacaze J, Herrrera M, Lesoult G. Precipitation path of secondary phases during solidification of the CoCrMoC alloy. Scr Mater 2002;47:811–6

[12] Sims CT. Contemporary view of cobalt-base alloys. J Met 1969;21:27–42

[13] A.R. Troiano and J.L. Tokich; “The transformation of Cobalt”; Tans. Amer. Inst. Min. Met. Eng. 175, pp. 728-741, (1948).

[14] Olson, G. B., and Morris Cohen. "A general mechanism of martensitic nucleation: Part I. General concepts and the FCC→ HCP transformation." Metallurgical Transactions A 7.12 (1976): 1897-1904.

[15] H. Lopez and A. J. Saldivar-Garcia. "Martensitic transformation in a cast Co-Cr-Mo-C alloy." Metallurgical and Materials Transactions A 39.1 (2008): 8-18

[16] A.J. Saldivar Garcia: Doctoral Thesis, CINVESTAV-IPN Unidad Saltillo, Saltillo, Mexico, 1998

[17] J.B. Vander Sande, J.R. Coke, and J. Wulff; “A Transmission Electron Microscopy Study of the Mechanisms of Strengthening in Heat Treated Co-Cr-Mo-C alloys”; Metallurgical Transactions A, Vol. 7A, pp.389-397. (March 1976)

[18] W. Rostoker and Dvorak; “Interpretation of Metallographic Structures”; 3rd edition; Academic Press Inc. ,(1990).

[19] A. Salinas-Rodriguez and J.L. Rodriguez-Galicia; “Deformation Behavior

of Low Carbon Co-Cr-Mo alloys for Low Friction Implant Applications”; Journal of Biomedical Materials Research, Vol. 31, pp. 409-419, (1996).

[20] Mani, A., and H. F. Lopez. "Deformation induced FCC to HCP transformation in a Co–27Cr–5Mo–0.05 C alloy." Materials Science and Engineering: A 528.7 (2011): 3037-3043.

[21] Kou, Sindo. Welding metallurgy. New York, 1987.

[22] Parvez, Shahid, et al. "Effect of Torch Angle on Arc Properties and Weld Pool Shape in Stationary GTAW." Journal of Engineering Mechanics 139.9 (2012): 1268-1277.

[23] Dilthey, Ulrich. Schweißtechnische fertigungsverfahren 2: verhalten der werkstoffe beim schweißen. Vol. 1. Springer DE, 2005

[24] Baer, Thomas M., and Mark S. Keirstead. "Nd-YAG laser." U.S. Patent No. 4,653,056. 24 Mar. 1987.

[25] Schlueter, H. O. L. G. E. R. "Laser beam welding." Welding journal 86.5 (2007): 37-39

[26] Ohno, Atsumi. The solidification of metals. Chijin Shokan Company, 1976.

[27] Jones, Denny A. Principles and prevention of corrosion. Prentice Hall, 1996.

[28] Sato, Norio. "Some concepts of corrosion fundamentals." Corrosion science 27.5 (1987): 421-433.

[29] Sato, N. (1976) passivity of Iron, Nickel, and Cobalt – General Theory of Passivity, in Passivity and its Breakdown on Iron and Iron Base Alloys (eds R. Staehle and H. Okada), NACE, Houston,pp. 1–9.

[30] F75-12Standard Specification for Cobalt-28 Chromium-6 Molybdenum Casting Alloy and Cast Products for Surgical Implants (UNS R30075). ASTM Book of standards, vol. 13.01, 2001.

[31] M.Sage and Ch. Guillaud; Revue de metallurgie, XLVII, No 2., 1950, pp139-145

[32] Kilner T, Pilliar RM, Weatherly GC, Alibert C. Phasei dentification and incipient melting in a cast CoCr surgical implant alloy. J Biomed Mater Res 1982;16:63–79.

[33] Giacchi, J. V., et al. "Microstructural characterization of as-cast biocompatible Co–Cr–Mo alloys." Materials Characterization 62.1 (2011): 53-61

[34] C. Montero, Ocampo, and A. Salinas Rodriguez:J. Biomed. Mater.Res., 1995, vol. 29, pp. 441-54

[35] A.J. Saldivar-Garcia, A. Mani-Medrano, A. Salinas-Rodriguez, Metall. Mater.Trans. A 30 (1999) 1177-1184.

[36] Kurosu, Shingo, Hiroaki Matsumoto, and Akihiko Chiba. "Isothermal Phase Transformation in Biomedical Co-29Cr-6Mo Alloy without Addition of Carbon or Nitrogen." Metallurgical and Materials Transactions A 41.10 (2010): 2613-2625.

[37] Zangeneh, Sh, M. Ketabchi, and H. F. Lopez. "Nanoscale carbide precipitation in Co-28Cr-5Mo-0.3 C implant alloy during martensite transformation." Materials Letters 116 (2014): 188-190.

[38] RajanK. Metallurgical Transactions A 1982; vol. 13; pp. 1161-6

[39] D.A. Porter and K.E. Easterling; “Phase Transformations in Metals and Alloys”; Cap. 3; Van Nostrand Reinhold (Iinternational). (1981).

[40] M. Browne, P.J. Gregson, Mateials Letters; vol. 24; (1995) pp. 1-6

[41] Hsu, Robert Wen-Wei, et al. "Electrochemical corrosion studies on Co-Cr-Mo implant alloy in biological solutions." Materials chemistry and physics 93.2 (2005): 531-538

[42] Cepeda-Rodríguez, F., et al. "Microstructural effects on the wear behavior ``of a biomedical as-cast Co-27Cr-5Mo-0.25 C alloy exposed to pulsed laser melting." Journal of Biomedical Materials Research Part A (2013).